Applications of Correlated Photon Pairs: Sub-Shot Noise Interferometry and Entanglement

by

Huanqian Loh

Submitted to the Department of Physics
in partial fulfillment of the requirements for the degree of

Bachelor of Science

at the

MASSACHUSETTS INSTITUTE OF TECHNOLOGY

June 2006

Author .....
Department of Physics
May 12, 2006

Certified by .....
Professor Vladan Vuletić
Lester Wolfe Associate Professor of Physics
Thesis Supervisor

Accepted by .....
Professor David E. Pritchard
Senior Thesis Coordinator, Department of Physics

Applications of Correlated Photon Pairs: Sub-Shot Noise Interferometry and Entanglement

by

Huanqian Loh

Submitted to the Department of Physics
on May 12, 2006, in partial fulfillment of the
requirements for the degree of
Bachelor of Science

Abstract

Using cesium atoms weakly coupled to a low-finesse cavity, we have generated photon pairs that are highly correlated in a non-classical way, as demonstrated by a large violation of the Cauchy-Schwartz inequality $G = 760^{+2100}_{-320}$ for a bin width $T = 60$ ns. Biphoton interferometry of the correlated pairs via the Holland-Burnett scheme [1] holds promise to demonstrate precision beyond the shot noise limit, although the current interference fringe visibility of $\beta = 0.84 \pm 0.04$ only translates to a shot noise limited phase uncertainty. Polarization-time entangled pairs can also be directly generated, by optically pumping the atoms to both $|F = 3, m_F = \pm 3\rangle$ ground states. The degree of entanglement, expressed by the calculated fidelity $f_\epsilon = 0.81 \pm 0.09$ and calculated Bell state parameter $S = 2.3 \pm 0.2$, is estimated to be finite but not maximal.

Thesis Supervisor: Professor Vladan Vuletić
Title: Lester Wolfe Associate Professor of Physics

Acknowledgments

This thesis is not a solo effort. Many people have contributed in one way or another towards the completion of this thesis, and it is my pleasure to acknowledge them here.

Adam Black built up much of the apparatus used in the cesium experiment. Although he had graduated by the time I joined that experiment, he showed me the ropes in my earlier projects, from soldering wires to aligning laser beams. Igor Teper and Yu-Ju Lin have been most helpful with their advice on assembling grating lasers and frequency noise measurements. Marko Cetina, Andrew Grier and Jonathan Campbell are always around to offer useful tips, and together with Haruka Tanji, Ian Leroux, Monika Schleier-Smith, Brendan Shields, Jacob Bernstein and Thaned Pruttivarasin, provide great companionship around the laboratory.

Of all the Vuletić group members, I am particularly indebted to three individuals who have been both fine mentors and fantastic labmates: Professor Vladan Vuletić, James Thompson and Jonathan Simon. Vladan has been truly inspiring as a research advisor. Besides providing invaluable guidance for my projects, he also exemplifies what it means to be a good physicist. James is one of the most nurturing figures I have met, while "cookie monster" Jon is simply an infectious bundle of energy around the laboratory. James' gift for explaining difficult concepts using the simplest pictures, combined with Jon's penchant for expressing physics in concrete equations, means that I have the best of both worlds when it comes to understanding physics. I would also like to thank Vladan, James and Jon for critically reading this manuscript.

Beyond the Vuletić group, I am grateful to members of the Ketterle group, who have been very generous on many occasions, such as the loan of their variable retarder. Special thanks go to Bonna Newman and my friends from New House 3, who have constantly reminded me to keep a balance between work and play. No amount of words can express my gratitude towards my family and Zilong Chen for their unwavering support and encouragement. Finally, I would like to acknowledge the Agency for Science, Technology and Research (A*STAR, Singapore) and Josephine de Kármán Fellowship for their support.

Contents

List of Figures

List of Tables

Chapter 1

Introduction

The single photon is the most basic ingredient in quantum optics. Single photon states can build up to form number states, or Fock states, which are conceptually simple for physicists to work with: a system described by the number state $|N\rangle$ contains only N photons. How can one obtain a single photon in the first place? One possible way is to excite a single atom, which in turn emits a single photon as it transitions to the ground state. However, it is not a trivial task to efficiently execute the single photon emission process in a controlled manner; typically, such a process is subject to Poisson statistics. What is instead desired is a "single photon gun" that can be "loaded" and "shot" at one's will.

It turns out that a cloud of cesium atoms, weakly coupled to a low-finesse cavity, can act as a conditional single photon source, as realized by the Vuletić group a few months before I joined the experiment [2, 6]. The procedure of "loading the gun" involves sending a highly attenuated "write" laser pulse through the atomic cloud, such that on average one atom is pumped into a different state $|1\rangle$ by the laser (and emits a "write photon" in the process; see Fig. 1-1). It is important that the atoms be collectively coupled to the cavity, so that the experimentalist is unable to tell which of the atoms had been excited. As long as any "which-atom" information remains unavailable, the "shooting" of the "single photon bullet" (i.e. the "read photon") can be accomplished with reasonable efficiency at some later time T_{wr}, when a "read" laser pulse pumps all the atoms back to the original state $|0\rangle$.

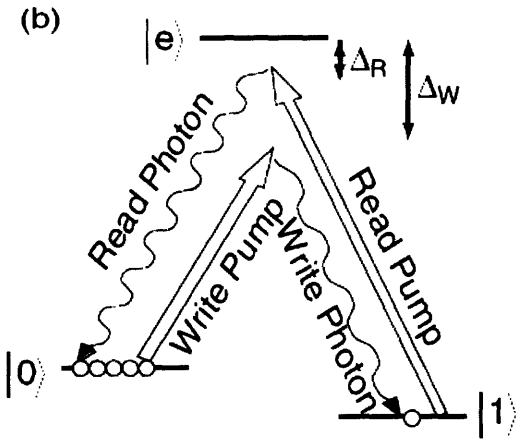

Figure 1-1: Atomic levels used in the conditional generation of single photons [2].

One can imagine modifying this idea of a conditional single photon source to obtain a photon pair source, by shortening the delay time T_{wr} between the application of the write and read laser pulses. In the limit where both the write and read laser beams are applied continuously, one might be able to generate continuous pairs of write and read photons! This is essentially the idea behind our present photon pair source, with some additional modifications to the single photon setup (e.g. using different atomic levels) that we shall not address for now.

Equipped with a source of photon pairs, one can perform a variety of experiments, such as sub-shot noise interferometry [7], tests of the Einstein-Podolsky-Rosen (EPR) paradox [8], and quantum cryptography [9]. One question, however, begs to be asked: given that correlated photon pairs have been produced since the advent of the parametric down converter (a non-linear crystal that outputs a pair of photons with frequencies that add up to the frequency of its input laser beam) in 1970 [10], what advantages do the Vuletić source of photon pairs provide over the parametric down converter?

The answer to the above question lies in the bandwidth of the photon pairs produced by the two sources. Pairs produced by parametric down converters tend to have broad frequencies, with widths on the order of 100 GHz [10]. Novel quantum communication schemes, however, require photon bandwidths on the order of 1 MHz

[11], which — surprise, surprise — the Vuletić source is able to provide!

Some of the most dramatic capabilities of our photon pair source are summarized in a paper submitted for publication [4]. One aim of this thesis is to provide intuitive pictures explaining the physics behind the generation of narrowband photon pairs in our setup. Chapter 3 gets to the heart of the physics by modeling the cloud of cesium atoms in a cavity as a three-level system. The experimental implementation and evidence for the correlated photon pairs are then described in Chapter 4. Two applications of the new photon pair source, which form the actual focus of my thesis work, are presented in Chapters 5 and 6. Chapter 5 describes a two-photon interference experiment that offers the potential to achieve sub-shot noise precision, while Chapter 6 shows how the collectively coupled atoms can serve as a resource for polarization-time entangled photons. Finally, Chapter 7 concludes with a summary and outlook of the atom-cavity system.

What about Chapter 2? In Chapter 2, we take a step back from all the excitement about photon pairs, and examine instead an important tool employed in almost every atomic physics experiment, including this one: the grating-tuned diode laser. Specifically, Chapter 2 describes the work I carried out to determine the influence of grating parameters on the linewidths of external-cavity diode lasers. For completeness, I have also included some linewidth measurements by Yu-Ju Lin and Marko Cetina, and Igor Teper's design of a diode laser mount with improved mechanical stability [12].

Chapter 2

Linewidths of Grating-Tuned Diode Lasers

2.1 Motivation and Background

Diode lasers have vast applications in atomic physics, because of their reliability, easy tunability, and low cost [13, 14]. Diode lasers alone, however, have linewidths of around 20 MHz [15], which are often too broad for manipulating atoms, and are typically not tunable to every wavelength of interest. Optical feedback, achieved by adding an external cavity element such as a diffraction grating, not only enhances the wavelength tunability, but also reduces the intrinsic linewidth to below 1 MHz [13]–[15].

Intrinsic linewidths of several hundred kHz are usually sufficiently narrow for most atomic physics experiments, since strong atomic transitions have typical linewidths of several MHz. However, certain experiments, such as cavity QED experiments [16], or those using narrow atomic transitions [17], require smaller laser linewidth. While it is possible to reduce the linewidth by actively stabilizing the laser to a high-finesse cavity with a fast servo loop [18], it is advantageous to prestabilize the laser by mechanical and optical design. From this practical viewpoint, we are interested in how various optical components in the grating laser setup — namely the grating, collimator and diode chip — affect the intrinsic laser linewidth. We have experimentally investigated

the linewidths of grating lasers in both the near IR (780 nm for Rb, 852 nm for Cs) and near UV (399 nm for Yb) regimes.

The linewidths of lasers have been extensively studied both theoretically [19]$^-$[25] and experimentally [26]$^-$[31]. Theoretical analysis of external cavity diode lasers shows that linewidths narrow with higher optical feedback. Most theoretical papers, however, model the external cavity element as a mirror without any frequency selectivity, instead of as a diffraction grating. Considering competition between diode chip modes as a mechanism for linewidth broadening [32, 33], we hypothesize that the linewidth should also depend on how well neighboring chip modes can be suppressed by the grating spectral profile, as characterized by the grating resolution. The latter is given by $\lambda/\Delta\lambda = mN_g = m(2D)/[(2/n_g)^2 - (\lambda m)^2]^{1/2}$, where m is the diffraction order, N_g is the number of illuminated grating lines, D is the beam diameter, λ is the wavelength, and n_g is the grating groove density. To our best knowledge, no study has so far been conducted to determine the effect of grating resolution on the linewidth. Furthermore, the influence of an antireflection (AR) coating on the front facet of the laser diode on the linewidth has not been as well studied as its effect on wavelength tunability. Wyatt has reported a significant effect of the AR coating on the linewidth of a 1.5 μm laser [28], while another experiment showed no effect for a 1.3 μm InGaAsP laser [29]. In the present work, we investigate how the linewidths of 780 nm and 852 nm grating-tuned diode lasers are influenced by the grating reflectivity, grating resolution and diode AR coating.

The conventional method for determining the linewidth is to superimpose two laser beams on a sufficiently fast photodiode, which yields the convolution of the spectral profiles of the two lasers. This method relies on the availability of a very narrow reference laser, so that the beat note frequency width mainly reflects the test laser linewidth. In addition, the intrinsic linewidth may sometimes be shrouded by low frequency mechanical vibrations, which may result in a broadened beat note. In this study, we have instead obtained the linewidth by measuring the power spectral density of the test laser's frequency noise fluctuations, $S(f)$. $S(f)$ is expected to display higher noise at low Fourier frequencies due to mechanical vibrations. The

noise then falls until it reaches a white noise level, S_0, at high Fourier frequencies [34]. S_0 is related to the intrinsic Lorentzian linewidth $\Delta\nu$ by [35]

$$\Delta\nu = \pi S_0^2. \tag{2.1}$$

To convert frequency noise into intensity noise that can be measured with a photodiode, either the transmission signal from a Fabry-Perot cavity [36, 37] or the atomic resonance line [34] can be used. The atomic line offers the advantage of being insensitive to mechanical vibrations. Using the atomic line to measure noise at low Fourier frequencies, we characterized an improved laser mount, a schematic of which is presented in the final section of this paper.

2.2 Frequency Noise Measurements

A typical grating laser used in this study is assembled in a Littrow configuration [14]. For each assembled laser, we carefully optimize its collimation and grating alignment to achieve the best possible optical feedback using the following procedure: monitoring the laser optical power, we set the laser diode current to just below its threshold value. The current is then dithered with a triangle wave of 100 Hz, and the onset of lasing manifests as a sudden increase in optical power with current. The goal is to minimize the laser threshold by adjusting the collimator position and the grating angle, assuming that the feedback is optimized when the threshold is minimized. The feedback is much more sensitive to the collimator position than to grating angle [3, 34].

Fig. 2-1 shows how the wavelength of an AR coated laser tunes with current for both optimized and unoptimized feedback. When the feedback is optimized, the wavelength tunes smoothly, with small jumps of 4.5 GHz between external cavity modes. On the other hand, when the vertical grating angle or the collimator lens is slightly misaligned, large frequency jumps of about 50 GHz appear, corresponding to lasing on different residual diode chip modes that have not been completely suppressed

due to imperfect AR coating.

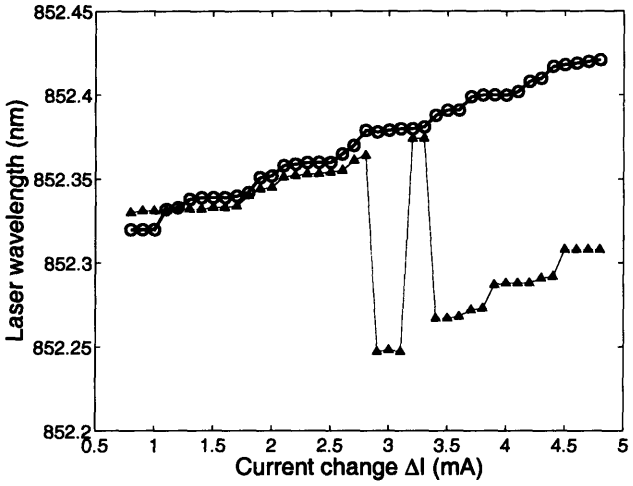

Figure 2-1: Tuning behavior of laser wavelength with current, for with (open circles) and without optimal (filled triangles) feedback, measured for an 852 nm laser diode with AR coating.

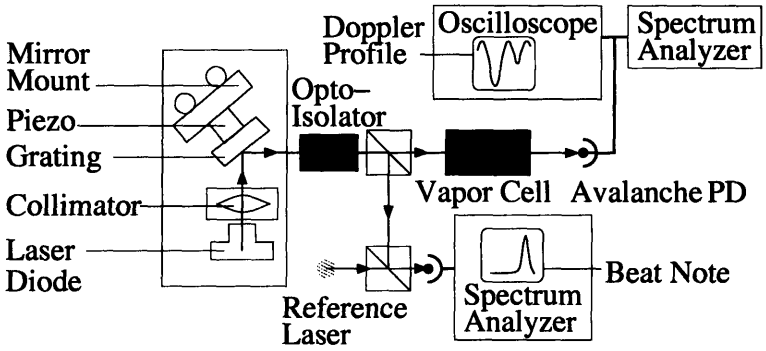

Figure 2-2: Schematic diagram of the setup used to measure laser frequency noise. Components like attenuators are not drawn. The polarization of the laser light is out of the plane.

Once the feedback is optimized, the laser light is sent through an atomic cell and onto an avalanche photodiode with a bandwidth of 300 kHz. The photodiode bandwidth is sufficient to measure the intrinsic linewidth, because the white frequency noise typically appears from Fourier frequencies of 20 kHz onwards. Fig. 2-2 shows a schematic of the setup used to measure the laser frequency noise. The laser wavelength is tuned to a value that matches the slope of a Doppler absorption profile (e.g. 852.334 nm for Cs), which allows us to use the atomic absorption line to convert the laser frequency noise into amplitude noise for detection by the avalanche

photodiode. For the 399 nm laser, the Dichroic Atomic Vapor Laser Lock (DAVLL) dispersive signal [38] from a hollow cathode lamp (Hamamatsu L2783-70HE-Yb) is used instead.

The slope of the absorption line is calibrated by beating the grating laser against a reference laser locked to another atomic cell. The slopes on the two sides of the absorption line are observed to be asymmetric, because of the linear increase in laser output power with wavelength. To remove this linear dependence, we average over measurements on both slopes of the atomic line.

The noise as measured by the avalanche photodiode in Fig. 2-2 contains both frequency noise and amplitude noise, which may or may not be correlated to each other. To measure the amplitude noise alone, we remove the atomic cell and insert gray filters to attenuate the beam power to its previous value on the photodiode. We find that the amplitude noise scales approximately as the square root of the power incident on the photodiode, an indication that the amplitude noise at the frequencies of interest is dominated by photon shot noise, and is thus uncorrelated with the frequency noise. Fig. 2-3 shows both the total noise and the amplitude noise contributions for a typical measurement. The frequency noise is obtained by subtracting the amplitude noise from the total noise in quadrature. The noise below 5 kHz generally reflects the mechanical vibrations of the laser mount, whereas the noise above 5 kHz becomes approximately independent of frequency, indicating a Lorentzian lineshape [35].

Applying Eq. (2.1) to the white noise portion, we measure typical linewidths of the 780 nm and 852 nm grating lasers to be in the 250–600 kHz range (see Tables 2.1 and 2.2). In fact, we also determine a similar linewidth of 250 kHz for a 399 nm Nichia NDHV310APC laser diode (non-AR coated) assembled with a 2400 mm^{-1} grating of reflectivity $R_1 = 0.60$.

For comparison, the method of converting frequency into amplitude noise via the atomic absorption line has allowed us to measure a linewidth as narrow as 30 kHz for a distributed Bragg reflector (DBR) laser diode, whose intrinsic linewidth was narrowed by optical feedback from a low-finesse optical cavity using a setup similar

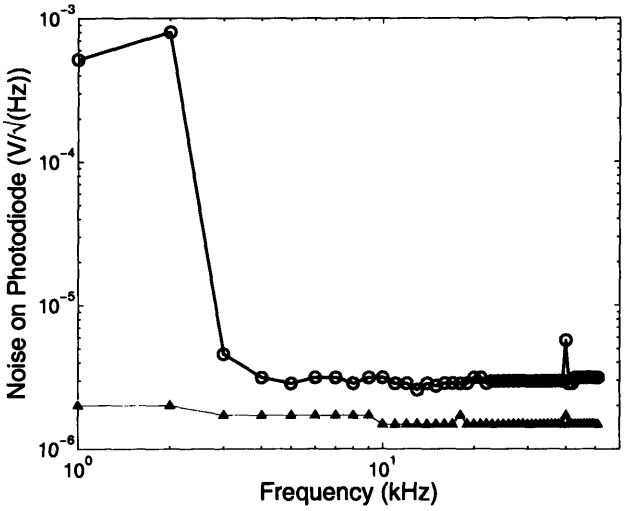

Figure 2-3: Total (open circles) and amplitude (filled triangles) spectral noise densities of an 852 nm AR coated laser assembled with a 1200 mm^{-1} grating of reflectivity $R_1 = 0.21$. For frequency noise, 1 $V/(Hz)^{1/2}$ corresponds to 156 $MHz/(Hz)^{1/2}$. For amplitude noise, 1 $V/(Hz)^{1/2}$ corresponds to a fractional noise of $0.94/(Hz)^{1/2}$.

to Dahmani[18] *et. al.*'s.

2.3 Effects of Grating Parameters and AR Coating on the Laser Linewidth

Table 2.1 shows the linewidths for various gratings (Edmund Optics 43222, 43753 and 43773) assembled with the same AR coated laser diode chip (Sacher Lasertechnik SAL-850-50-SDL) and collimator (Thorlabs C390TM-B, effective focal length = 2.75 mm).

As expected from theory, the higher the grating reflectivity R_1, the narrower the linewidth. We also note, from comparing the first and third rows of Table 2.1, that the linewidth narrows with higher grating resolution despite a lower grating reflectivity. Fig. 2-4 gives a physical picture accounting for both effects of grating reflectivity and resolution. The external cavity, formed between the back facet of the laser diode chip and the reflective grating surface, is modeled as a passive Fabry-Perot cavity, whose finesse is first maximized during the feedback optimization procedure described above. Its highest achievable finesse, however, is limited by the reflectivity of the grating

Table 2.1: Linewidths of 852 nm lasers built with different gratings.

Grating part number	R_1	R_0	n_g (mm^{-1})	$\lambda/\Delta\lambda$	$\Delta\nu$ (kHz)
43773	0.21	0.67	1200	4200	560 ± 140
43753	0.61	0.19	1200	4200	440 ± 110
43222	0.16	0.78	1800	8400	320 ± 60

Linewidths of AR coated 852 nm lasers built with gratings (from Edmund Optics) of different reflectivities into the first and zeroth diffraction orders R_1 and R_0 respectively, and different groove densities n_g. For a Littrow grating laser, the first diffraction order is reflected back into the laser for optical feedback, while the zeroth order is used as the laser output. R_1 and R_0 are measured values, while the grating resolution $\lambda/\Delta\lambda$ is computed for a beam diameter of $D \simeq 3$ mm.

chosen. The grating resolution, on the other hand, sets the width of the grating profile in Fig. 2-4. A higher grating resolution, achieved with a grating of higher groove density or a collimator that produces larger beam size, better suppresses neighboring diode chip modes, leading to less mode competition and hence less frequency noise. In fact, the greater influence of the grating resolution on the linewidth reduction indicates that the suppression of other laser diode chip modes is more important than the finesse of the external cavity.

The results in Table 2.1 imply that one may be able to obtain a narrower linewidth by simply using a grating of higher groove density, while keeping the zeroth order reflectivity R_0 and laser output power high. In addition, we attempted to increase the grating resolution by using a collimator that produced a larger beam size (Thorlabs C240TM-B, effective focal length = 8.0 mm). We found that even when the optical feedback was only near-optimized, we could already achieve a linewidth of 425 kHz using the 1800 mm^{-1} grating. On the other hand, the combination of the larger beam size and 1800 mm^{-1} grating also means that the optical feedback is much more sensitive to the grating angle. At such high sensitivity, slight thermal drifts of the aluminum laser mount made it extremely difficult for the grating to remain at its optimal angle. As a result, we were unable to maintain reliable operation in the mechanical setup of Fig. 2-2 for this collimator-grating combination.

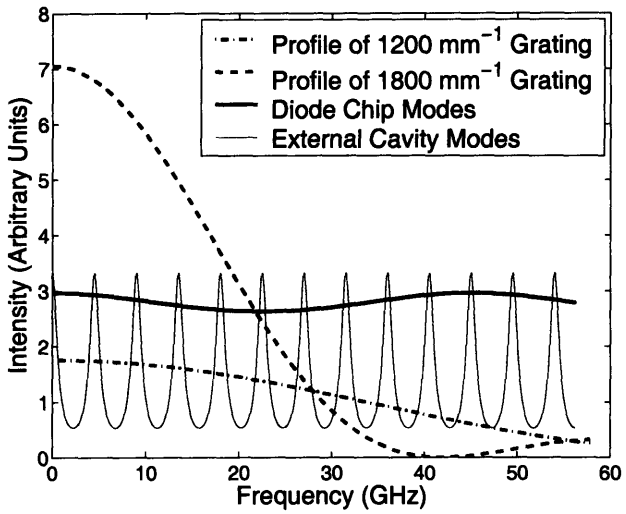

Figure 2-4: Calculated profiles of 1200 mm^{-1} and 1800 mm^{-1} gratings, overlapped with diode chip and external cavity modes spaced by frequency intervals determined from Fig. 2-1. The width of the passive external cavity mode is calculated for a grating of reflectivity $R_1 = 0.61$ and diode chip back facet reflectivity[3] ≈ 0.3. The width of the passive diode chip mode is calculated for an AR coated diode chip with the above back facet reflectivity and front facet reflectivity[3] ≈ 0.003.

We also study the effect of an AR coating on the linewidth. Table 2.2 shows the linewidths of AR coated and uncoated laser diodes assembled with the same grating ($R_1 = 0.27, n = 1200$ mm^{-1}). Although the AR coated laser has a slightly narrower linewidth, the estimated error bar associated with each measurement is approximately 100 kHz. We hence conclude that although the AR coating eases the procedure for optimizing grating alignment as well as enhances wavelength tunability (Fig. 2-1), its effect on the linewidth is insignificant.

Table 2.2: Linewidths of both AR and non-AR coated 780 nm lasers.

Diode Model	AR Coating	$\Delta\nu$ (kHz)
Sanyo DL7140-201	No	500 ± 100
SAL-780-40	Yes	450 ± 100

Linewidths of 780 nm lasers with and without an AR coating on the front facet. A grating (Edmund Optics 43773; see Table 2.1) is used.

The linewidth error bar of 100 kHz is estimated from the fact that the amount

of current injected into the diode laser influences the extent to which the laser operates in a single mode, which in turn affects the linewidth (Fig. 2-5). When the laser is about to jump to a different mode, it becomes slightly multi-mode and the linewidth increases by an order of magnitude due to mode competition. Although we have verified that the laser operated in a single mode during our frequency noise measurements, Fig. 2-5 shows that there is still a linewidth variation of about 80 kHz in the single-mode regime.

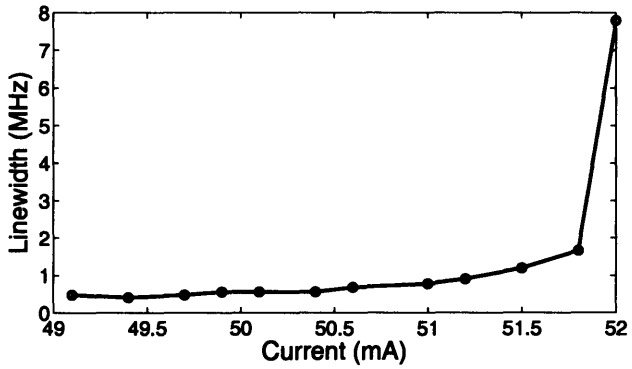

Figure 2-5: Plot of linewidth versus current injected into the diode laser. The laser jumps to a different longitudinal cavity mode near 52 mA.

Table 2.3 summarizes the smallest linewidths obtained for the near IR diode lasers (780 nm, 852 nm). For comparison, the linewidth of the near UV laser (399 nm) is included.

Table 2.3: Best achieved linewidths of 852 nm and 780 nm lasers.

Atoms	λ (nm)	AR Coating	R_1	n_g (mm^{-1})	$\lambda/\Delta\lambda$	$\Delta\nu$ (kHz)
Cs	852	Yes	0.16	1800	8400	320 $\pm$ 60
Rb	780	Yes	0.27	1200	4100	450 $\pm$ 100
Yb	399	No	0.60	2400	8200	250 $\pm$ 70

Smallest achieved linewidths of 852 nm and 780 nm lasers and their corresponding diode and grating parameters. For comparison, the linewidth of the 399 nm laser is listed.

2.4 Mechanical Stability of Laser Mounts

Fig. 2-6 shows a new laser mount ("mount B") that is designed to reduce mechanical oscillations at higher acoustic frequencies. For the regular mount[14] ("mount A"; see Fig. 2-2), the grating and laser diode are separately attached to a third aluminum piece that serves as the base of the mount. The vertical and horizontal grating angles are adjusted by turning the screws of the mirror mount. Conversely, for mount B, the aluminum block containing the grating is attached directly to the block containing the laser diode via four nylon pull screws. Three stainless steel screws, which push on a rubber ring and a piezo stack sandwiched between the two blocks, respectively, allow the vertical and horizontal grating angles to be adjusted with better resolution. In fact, the vertical angle only needs to be adjusted slightly, because the optical feedback is already near-optimal when the grating sits flush in the machined pocket. Mount B also includes a mirror, which couples the beam out of the mount in a fixed direction regardless of the grating's horizontal angle [39].

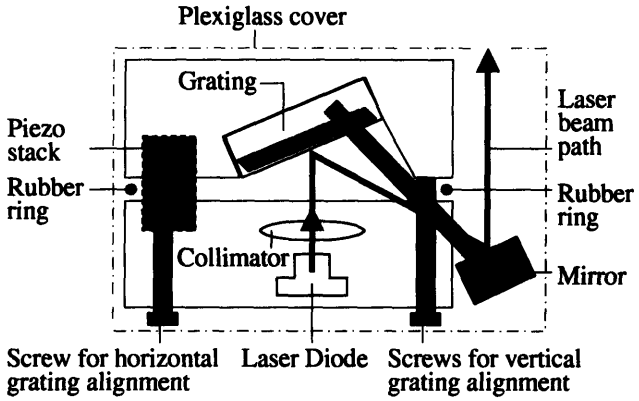

Figure 2-6: Schematic diagram of mount B. The four nylon pull screws that attach the two aluminum blocks to each other are not drawn.

The mechanical properties of mount B are characterized in terms of its frequency noise power spectral density and root-mean-square (RMS) jitter at low Fourier frequencies (up to 5 kHz), and are plotted in Fig. 2-7 and 2-8 respectively. For comparison, Fig. 2-7 and 2-8 also display the data for a laser assembled with mount A. At first glance, mount A appears to be more stable than mount B, because its overall noise is lower. However, the low frequency noise can often be easily reduced with a

feedback circuit. In fact, the lower the frequencies at which resonances occur, the easier it is for the feedback circuit to compensate for noise. In this respect, mount B is better than mount A, because its mechanical resonance only occurs at 500 Hz, whereas mount A has resonances at around 2 kHz. As shown in Fig. 2-8, the RMS jitter of the laser built with mount B is much lower than that for mount A, when both lasers are locked. Integrating from 0 Hz up to a bandwidth of $f = 10$ kHz, we achieve RMS jitters of $\Delta\nu_{\text{jitter}}(f) = [\int_0^f (S(f'))^2 df']^{1/2} = 40$ kHz and 100 kHz for the actively stabilized lasers built with mounts B and A, respectively.

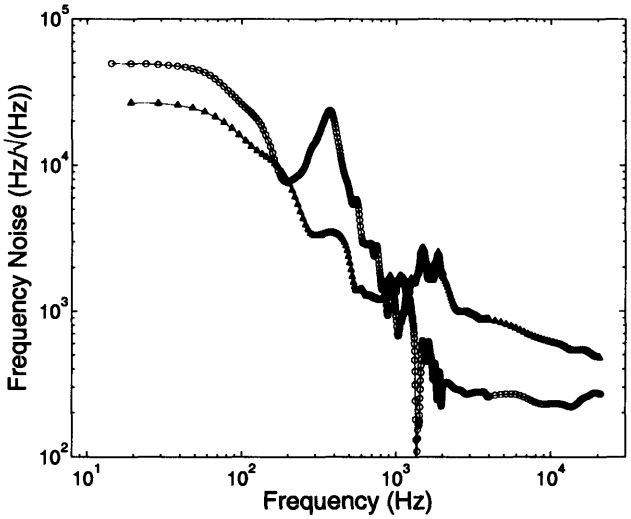

Figure 2-7: Frequency noise power spectral densities for mount B (open circles) and mount A (filled triangles) lasers. Mount B only has a mechanical resonance at 500 Hz, whereas mount A has mechanical resonances at 2 kHz.

2.5 Summary of Linewidth Studies

We have measured frequency noise power spectral densities to determine laser linewidths for various grating laser setups. We find typical linewidths of 250–600 kHz for lasers operating near 399 nm, 780 nm and 852 nm. The linewidth depends on the type of grating and collimator. The presence of an AR coating has an insignificant effect on the linewidth reduction, but enhances tuning stability. On the other hand, the higher the grating reflectivity and grating resolution, the narrower the linewidth. In particular, the grating resolution has a larger effect on the linewidth than the grating

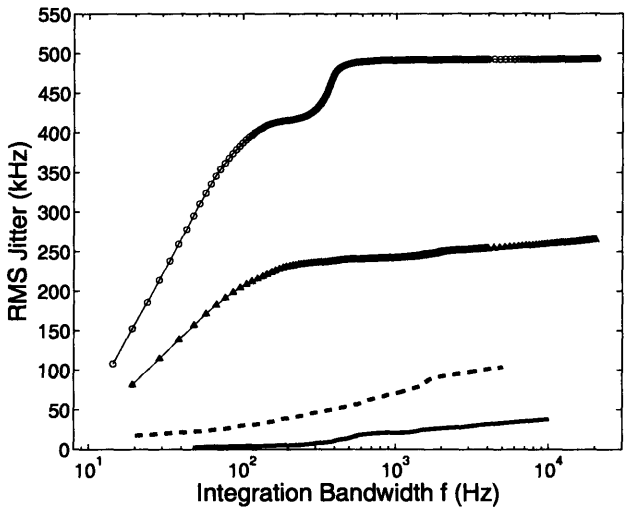

Figure 2-8: RMS jitters of lasers assembled both with mount B (open circles for unlocked and solid line for locked) and mount A (filled triangles for unlocked and dashed line for locked). The RMS jitter is given by $\Delta\nu_{\text{jitter}}(f) = [\int_0^f (S(f'))^2 df']^{1/2}$.

reflectivity.

Using a new laser mount with improved mechanical properties, we were able to achieve an RMS jitter of 40 kHz for an actively stabilized system with a loop bandwidth of only 1.5 kHz.

Chapter 3

Cesium Atoms in a Cavity: a Three-Level System

3.1 Atomic Transitions Used in Cesium

Chapter 1 has already provided a brief introduction to the idea behind generating pairs of write and read photons. Fig. 3-1 shows the relevant cesium energy levels that the π-polarized write and read laser pumps interrogate to produce the corresponding write (σ^+-polarized) and read (σ^--polarized) photon pairs. For convenience, we denote the atomic states as the following: $|a\rangle \equiv |F = 3, m_F = -3\rangle$, $|b\rangle \equiv |F' = 3, m'_F = -3\rangle$, $|f\rangle \equiv |F = 3, m_F = -2\rangle$, $|e\rangle \equiv |F' = 2, m'_F = -2\rangle$, where F, F' are quantum numbers that label the ground state $6^2S_{1/2}$ and excited state $6^2P_{3/2}$ respectively. Because all the atoms are optically pumped to $|a\rangle$ initially, the read process ($|f\rangle \rightarrow |e\rangle \rightarrow |a\rangle$) can only take place after the write process transfers an atom from $|a\rangle$ to $|f\rangle$. The write process, however, can "reverse" itself as the interrogated atom Rabi-flops from $|f\rangle$ back to $|a\rangle$ via $|b\rangle$. To reduce competition between the read and reverse-write processes, we use a far-detuned write laser pump and an on-resonance read laser pump. Since the spontaneous emission rate goes as the inverse-square of the laser detuning δ for large δ [40], the read process occurs much more quickly than the reverse-write process.

The above comparison of the write and read rates gives us a better understanding

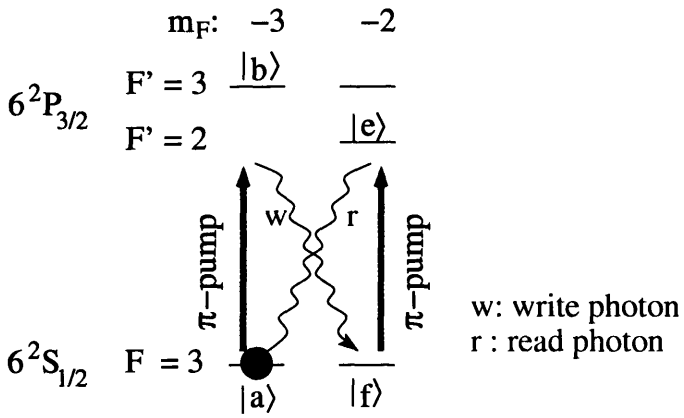

Figure 3-1: Atomic levels used in the generation of photon pairs. The write pump beam is red-detuned from atomic resonance by $\delta = 150$ MHz.

of how the read photon can be generated conditionally on the write photon. However, the ability to generate photon pairs does not necessarily translate into the ability of detecting photon pairs! The issue is that an excited atom emits a photon into 4π steradians when it makes a transition back to the ground state. Unless we had a special device that could collect the photons emitted into all possible solid angles, we would have a very low detection efficiency, limited by $\Delta\Omega_{det}/4\pi$, where $\Delta\Omega_{det}$ is the solid angle subtended by the detector.

The low-finesse, single-mode cavity that the cloud of cesium atoms are weakly coupled to provides an alternative solution to the special detecting device. Instead of collecting photons emitted into 4π steradians, the cavity enhances the emission of photons into its single cavity mode [41]. The photons then leak out of the cavity at a rate given by the cavity linewidth κ into a detector outside of the cavity. To develop a common language describing the coupling of the cesium atoms to the cavity, the concept of a single atom's cooperativity η to the cavity mode will now be introduced.

3.2 Cooperativity Parameter

The cooperativity parameter η describes how well a single atom can emit a photon into one direction of a single cavity mode compared to that into free space. From geometrical considerations, η goes as the ratio of the solid angle subtended by the

cavity mirror $\Delta\Omega_c$ to 4π, and is enhanced by the cavity finesse $\mathcal{F}$. $\Delta\Omega_c/4\pi$ in turn goes as $(\lambda/w_c)^2$, which can be thought of as the number of photons of wavelength λ that can "fit" into an area characterized by the cavity mode waist w_c. Putting in all the numerical factors, we get [41, 42]:

$$\eta = \frac{3}{2\pi^3}\mathcal{F}\left(\frac{\lambda}{w_c}\right)^2 . \tag{3.1}$$

Fig. 3-2 offers a different perspective on the cooperativity parameter. The levels depicted in Fig. 3-2 correspond to an atom in the excited state (in our case, $6^2P_{3/2}$) with no photons in the cavity $|\mathbf{e}, 0\rangle$, and an atom in the ground state ($6^2S_{1/2}$) with one photon in the cavity $|\mathbf{g}, 1\rangle$. The two levels are coupled by a Rabi frequency g, which is the single-atom vacuum Rabi frequency as extracted from the Jaynes-Cummings model [43]. For an atom initialized in $|\mathbf{e}, 0\rangle$, η is given by the probability of emitting a κ-photon into the cavity mode compared to that of emitting a Γ-photon into free space:

$$\eta = \frac{g^2/\kappa}{\Gamma} = \frac{g^2}{\kappa\Gamma} . \tag{3.2}$$

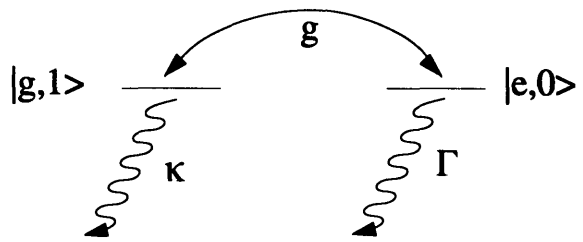

Figure 3-2: Two-level system of an atom coupled to a cavity. The first label (**e**, **g**) denotes whether the atom is in the excited or ground state. The second label denotes the number of photons in the cavity. κ is the cavity linewidth and Γ is the natural linewidth of the $|\mathbf{e}\rangle \rightarrow |\mathbf{g}\rangle$ transition.

Both expressions for η turn out to be equivalent, although Eq. (3.2) is more convenient for explaining the physics in the following sections. Ideally, we would like η to be as large as possible, so as to achieve a high directionality in the emission of the write or read photon. On the other hand, it is technically challenging to strongly couple a single atom to a high-finesse cavity with a small mode waist. The way we

circumvent this problem is to collectively couple N_a atoms to a cavity. As long as $N_a\eta \gg 1$, a photon will be emitted into the cavity mode with a high likelihood, even for the case of a low-finesse cavity.

3.3 Superradiance on the Read Process

For the write process, achieving $N_a\eta \gg 1$ is trivial: the factor N_a comes from the fact that there are initially N_a atoms in the ground state, all of which can be possibly excited. Meeting the same condition $N_a\eta \gg 1$, however, is not as intuitive for the read process. Afterall, when the read process is initialized, only one atom will be in $|f\rangle$ (see Fig. 3-1)! How then does the read photon get preferentially emitted into the cavity mode?

The trick is that the write process must drive an atom from $|a\rangle$ to $|f\rangle$ in a way that the experimentalist is unable to tell which atom had made the transition. Eq. (3.3) show the states used in the read process, including now an additional label for the number of read photons in the cavity $|n_r\rangle$ (see also Fig. 3-3). Because the atom that is driven to $|f\rangle$ cannot be identified, one must symmetrize the states of the read process [44, 45]:

$$|F\rangle \equiv \frac{1}{\sqrt{N_a}}\sum_{i=1}^{N_a}\prod_{j\neq i}|f_i\ a_j\rangle\,|0_r\rangle \equiv \frac{1}{\sqrt{N_a}}\sum_{i=1}^{N_a}|f_i\rangle\,|0_r\rangle\ , \tag{3.3a}$$

$$|E\rangle \equiv \frac{1}{\sqrt{N_a}}\sum_{i=1}^{N_a}\prod_{j\neq i}|e_i\ a_j\rangle\,|0_r\rangle \equiv \frac{1}{\sqrt{N_a}}\sum_{i=1}^{N_a}|e_i\rangle\,|0_r\rangle\ , \tag{3.3b}$$

$$|G\rangle \equiv \prod_{i=1}^{N_a}|a_i\rangle\,|1_r\rangle \equiv |a\rangle\,|1_r\rangle\ . \tag{3.3c}$$

Since the $j \neq i$ atoms are always sitting in $|a\rangle$, the labels $|a_j\rangle$ are dropped for convenience.

The on-resonance Rabi frequencies that couple the symmetrized read states are

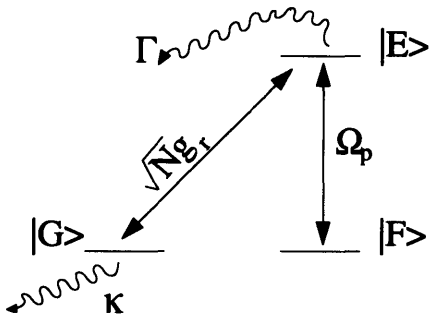

Figure 3-3: Atom-cavity states, couplings and rates of decay involved in the read process.

then given by the following expressions:

$$\Omega_{FE} = \Omega_p , \tag{3.4a}$$

$$\Omega_{EG} = \sqrt{N_a} g_r , \tag{3.4b}$$

where Ω_p is the Rabi frequency of the read pump beam interacting with one atom. The expression for Ω_{FE} comes as no surprise, for only one atom is making the atomic transition $|f\rangle \rightarrow |e\rangle$. The scaling of Ω_{EG} with the square root of the number of atoms, however, is unexpected. The following equation provides a more careful computation of Ω_{EG}:

$$\begin{aligned}
\Omega_{EG} &\equiv -\frac{1}{\hbar} \left\langle G \left| \vec{d} \cdot \vec{E} \right| E \right\rangle \\
&= \left\langle G \left| g_r (\hat{\sigma}_+ \hat{a} + \hat{a}^\dagger \hat{\sigma}_-) \right| E \right\rangle \\
&= \frac{g_r}{\sqrt{N_a}} \sum_{i=1}^{N_a} \left\{ \langle a | \langle 1_r | \right\} \left(\hat{\sigma}_+ \hat{a} + \hat{a}^\dagger \hat{\sigma}_- \right) \left\{ |e_i\rangle |0_r\rangle \right\} \\
&= \frac{g_r}{\sqrt{N_a}} N_a \\
&= \sqrt{N_a} g_r .
\end{aligned} \tag{3.5}$$

The first and second lines in the above equation rewrite the usual Hamiltonian for a two-level atom interacting with an electric field $-\vec{d} \cdot \vec{E}$ in terms of the read photon creation $\hat{a}^\dagger$ and annihilation $\hat{a}$ operators, and operators describing the $|a\rangle \leftrightarrow |e\rangle$ atomic transitions i.e. $\hat{\sigma}_+ = |e\rangle\langle a|$ and $\hat{\sigma}_- = |a\rangle\langle e|$ [43]. Simply put, the term $\hat{\sigma}_+ \hat{a}$

takes an atom from $|a\rangle$ and puts it in $|e\rangle$ while absorbing a read photon from the cavity mode, and vice versa for $\hat{a}^\dagger\hat{\sigma}_-$. The last few lines of the calculation tell us that the $\sqrt{N_a}$ factor comes from coupling a symmetrized state to a product state upon the emission of a read photon. Returning to Fig. 3-2 with $\Omega_{EG} = \sqrt{N_a}g_r$ instead of merely g_r, we find the cooperativity for the emission of the read photon to be

$$\frac{(\sqrt{N_a}g_r)^2/\kappa}{\Gamma} = N_a\frac{g_r^2}{\kappa\Gamma} = N_a\eta\,. \tag{3.6}$$

Eq. (3.6) shows that the read photon is N_a times more likely to be emitted into the cavity mode than expected for a single atom in the excited state. Such collective enhancement of spontaneous emission is also known as Dicke superradiance [44].

3.4 Four-Wave Mixing

Up to this point, we have ignored in our discussion of superradiance the finite spatial extent of the atomic cloud. Since the cloud of atoms is larger than the wavelength of the emitted photons, a spatial phase-matching condition must also be fulfilled to achieve superradiance [44]:

$$\vec{P}_{r,photon} = \vec{P}_{w,pump} - \vec{P}_{w,photon} + \vec{P}_{r,pump} \tag{3.7}$$

Fig. 3-4 illustrates the phase-matching condition, where $\vec{P}$ is the momentum of the photon indicated in the subscript. In our case, the phase-matching condition is satisfied by retro-reflecting the write pump beam to produce the read pump beam.

Since the momenta sum to zero, and the initial and final states of the system remain the same (i.e. all atoms in $|a\rangle$), the generation of the write and read photon pair can be viewed as a four-wave mixing process. In the language of four-wave mixing, we now have another picture for the superradiant emission of the read photon: the incoming write pump beam and the outgoing write photons interfere to form a spin grating in the atomic cloud (depicted by the dashed lines in Fig. 3-4). The incoming read pump beam then scatters off the atomic grating to give outgoing read photons.

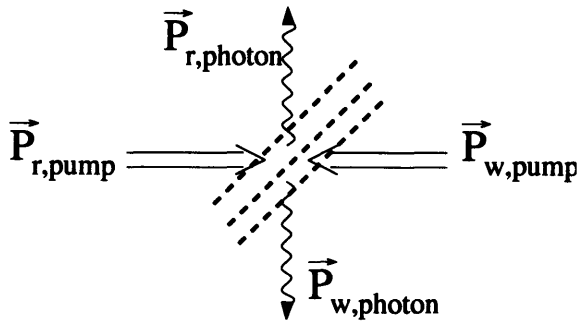

Figure 3-4: Momenta of write and read laser pumps, which generate the write and read photons respectively. The write and read laser pumps are aligned to be counter-propagating, whereas the write and read photons are emitted into the cavity mode. The dashed lines depict the spin grating obtained from interfering the write pump and emitted write photons.

Because it is N_a times as likely for a write photon to be scattered into the cavity mode, the emission of the read photon into the cavity is also enhanced by N_a. (The emission of the write and read photons into opposite directions does not matter, because both photons will circulate within the cavity anyway.)

3.5 Three-Level System Dynamics on the Read Process

Superradiance, while a rich phenomenon itself, does not give the full physics associated with the read process. Instead of focusing on the coupling between states $|E\rangle$ and $|G\rangle$, we return to the full three-level system depicted in Fig. 3-3.

The reader is reminded that the couplings Ω_{FE} and Ω_{EG} occur on atomic resonance. For the moment, we shall ignore the fact that photons can decay out of the system via κ and Γ. Using the interaction picture in the $\{|F\rangle, |E\rangle, |G\rangle\}$ basis, the three-level system can then be described by the Hamiltonian

$$H = \hbar \left[\frac{\Omega_p}{2} \left(|F\rangle\langle E| + |E\rangle\langle F| \right) + \sqrt{N_a} g_r \left(|G\rangle\langle E| + |E\rangle\langle G| \right) \right], \tag{3.8}$$

with eigenvalues and eigenstates

$$\begin{aligned} E_I &= \hbar\Omega' : \quad |I\rangle = \tfrac{1}{\sqrt{2}\Omega'}(\tfrac{\Omega_p}{2}|F\rangle + \Omega'|E\rangle + \sqrt{N_a}g_r|G\rangle), \\ E_{II} &= -\hbar\Omega' : \quad |II\rangle = \tfrac{1}{\sqrt{2}\Omega'}(\tfrac{\Omega_p}{2}|F\rangle - \Omega'|E\rangle + \sqrt{N_a}g_r|G\rangle), \\ E_{III} &= 0 \quad : \quad |III\rangle = \tfrac{1}{\Omega'}(\sqrt{N_a}g_r|F\rangle - \tfrac{\Omega_p}{2}|G\rangle), \end{aligned} \tag{3.9}$$

where $\Omega' = [(\Omega_p/2)^2 + N_a g^2]^{1/2}$. Note that the third eigenstate is special: it has no excited state component. In conventional three-level physics terminology, $|III\rangle$ is also known as the dark state, because it cannot spontaneously emit any photons by making a transition from $|E\rangle$ to any of the two ground states [43].

We now allow the read photon to leave via κ and Γ decay, as the system transitions back to a fourth level $|A\rangle \equiv \prod_{i=1}^{N_a}|a_i\rangle|0_r\rangle$. The master equation approach gives the most general description of the system [43, 46]:

$$\begin{aligned} \dot{\rho} &= \frac{1}{i\hbar}[H,\rho] + \Gamma|A\rangle\langle E|\rho|E\rangle\langle A| + \kappa|A\rangle\langle G|\rho|G\rangle\langle A| \\ &\quad -\frac{\Gamma}{2}(|E\rangle\langle E|\rho + \rho|E\rangle\langle E|) - \frac{\kappa}{2}(|G\rangle\langle G|\rho + \rho|G\rangle\langle G|)\,, \end{aligned} \tag{3.10}$$

where H is the Hamiltonian from Eq. (3.8) and ρ is the density matrix of the four-level system. It turns out that, because the κ and Γ photons decay out of the three-level system, the four-level master equation approach is equivalent to the Schrödinger wavefunction approach for a modified three-level interaction Hamiltonian:

$$i\hbar\dot{\psi} = H'\psi\,, \quad H' = H - i\hbar(\frac{\Gamma}{2}|E\rangle\langle E| + \frac{\kappa}{2}|G\rangle\langle G|)\,, \tag{3.11}$$

where ψ is the wavefunction of the system.

Under the modified Hamiltonian, the states $|E\rangle$ and $|G\rangle$ have some imaginary width corresponding to their decay rates. In the basis of eigenstates, Γ has no effect on the dark state, although it pulls the other two eigenenergies E_I and E_{II} closer to each other [47]. On the other hand, κ "spoils" the dark state by coupling some excited state component into $|III\rangle$. Returning to our original goal of photon pair generation, we see that we would like as many photons to leave from $|G\rangle$ as possible, instead of

losing them via Γ-decay from $|E\rangle$. Therefore, to achieve a high recovery efficiency of the read photon, we need to be well-overlapped with the "almost-dark" state $|E_{III}\rangle$, which is also the state with the least (albeit finite) excited state component.

We expect the read photons to be emitted with an exponential decay in time (where initial time is defined to be that when a write photon is emitted into the cavity) if the overlap with the almost-dark state is perfect. Otherwise, the admixture of other eigenstates shows up as Rabi-flops in the time-dependent emission of the read photons, as simulated in Fig. 3-5.

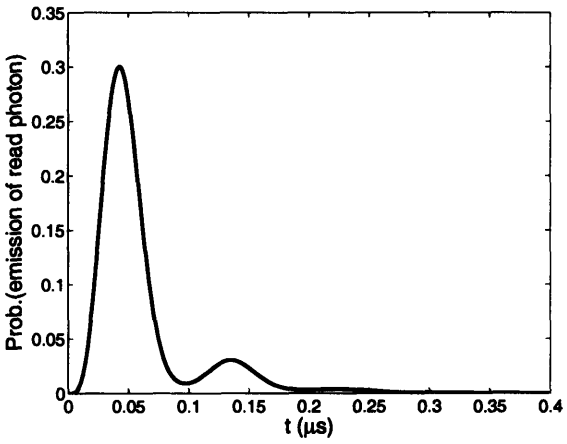

Figure 3-5: Time-dependent probability for the read photon to be emitted into the cavity, where $t = 0$ is the time when a write photon is emitted into the cavity.

When a write photon is emitted into the cavity, the system is initialized in a superposition of all three read eigenstates. How then can the system have a strong overlap with the almost-dark state? In our experiment, the frequency of the single cavity mode has been tuned to coincide with atomic resonance. Because $E_{III} \approx 0$, the write cavity mode is nearly resonant with the almost-dark state, while the other eigenenergies E_I and E_{II} are filtered out by the frequency width of the write cavity (see Fig. 3-6). Hence, as the write photon leaks out of the cavity and into the detector, the phases of the two "bright" eigenstates $|I\rangle, |II\rangle$ cancel out, and what remains is a coherent overlap with the almost-dark state $|III\rangle$.

In the time domain, the cavity filtering of the write photons is equivalent to convolving the *amplitude* of read photon emission $\langle G|\psi(t)\rangle$ with the *amplitude* of write

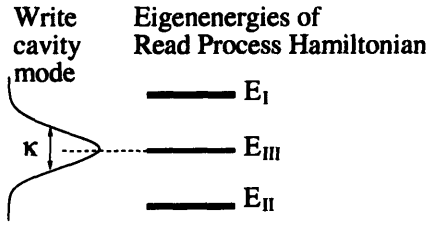

Figure 3-6: Cavity filtering of the write photon results in good overlap with the almost-dark state $|III\rangle$ for the read process.

photons decaying out of the cavity $e^{-(\kappa/2)t}$. It is important that the convolved quantities be amplitudes instead of probabilities, for the following reason: both $\langle G|\psi(t)\rangle$ and $e^{-(\kappa/2)t}$ have $t = 0$ defined as the time when a write photon is emitted into the cavity. However, there is no way of finding out when a write photon is actually emitted into the cavity without making a measurement that disturbs the system dynamics. Our knowledge of when the read photon is emitted is smeared out by the time over which the write photon leaves the cavity for the detector, therefore one can only add amplitudes instead of probabilities. In other words, the above convolution of amplitudes is analogous to the Feynman path integral [48], where the "paths" in this case are indistinguishable time paths for the write photon to be emitted. Fig. 3-7 shows the result of convolving Fig. 3-5 with $e^{-(\kappa/2)t}$, which is the time dependent probability of emitting a read photon into the cavity, where initial time is now defined to be that when a write photon has left the cavity.

3.6 Write Process

We examine the mechanism responsible for initializing the read process: the write process. Like in the read process, there are three states involved in the write process

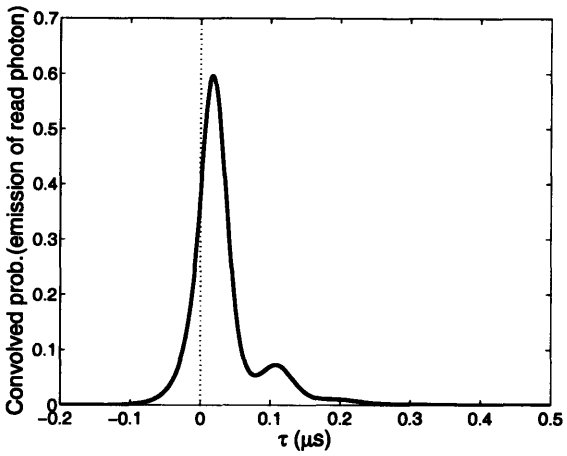

Figure 3-7: Time-dependent probability for the read photon to be emitted into the cavity, where $t = 0$ is the time when a write photon has left the cavity.

(see Fig. 3-8a):

$$|A\rangle \equiv \prod_{i=1}^{N_a} |a_i\rangle\,|0_w\rangle\ , \tag{3.12a}$$

$$|B\rangle \equiv \frac{1}{\sqrt{N_a}} \sum_{i=1}^{N_a} \prod_{j\neq i} |b_i\ a_j\rangle\,|0_w\rangle\ , \tag{3.12b}$$

$$|C\rangle \equiv \frac{1}{\sqrt{N_a}} \sum_{i=1}^{N_a} \prod_{j\neq i} |f_i\ a_j\rangle\,|1_w\rangle\ . \tag{3.12c}$$

The Rabi frequencies coupling the states are $\Omega_{AB} = \sqrt{N_a}\omega_p$ and $\Omega_{BC} = g_w$, where ω_p is the Rabi frequency of the write pump beam interacting with one atom.

One key difference between the two processes is the fact that all N_a atoms start in the $|a\rangle$ state, which is to be contrasted with only one atom starting in the $|f\rangle$ state for the read process. Another major distinction is that the write laser is red-detuned by $\delta = 150$ MHz from atomic resonance. The large detuning ($\delta \gg \Omega_{AB}, \Omega_{BC}$) allows us to simplify the three-level system into a two-level one, where the two levels $|A\rangle$ and $|C\rangle$ are coupled by an effective two-photon Rabi frequency (see Fig. 3-8b):

$$\Omega_{eff} = \frac{\sqrt{N_a}\omega_p g_w}{2\delta}. \tag{3.13}$$

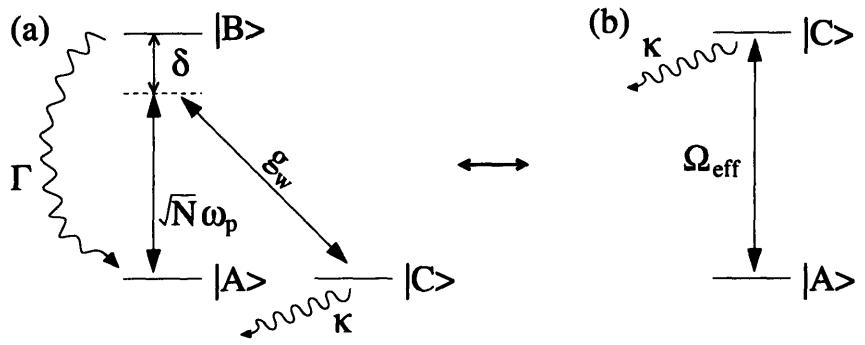

Figure 3-8: (a) Atom-cavity states, couplings, and rates of decay involved in the write process. (b) The two-level system that effectively describes the write process, in the limit of large laser detuning δ.

The write photon then leaks out from $|C\rangle$ via κ decay. Note that Γ does not enter the description of the effective two-level system, because the system is merely reinitialized in $|A\rangle$ when the excited atom decays back to its ground state $|a\rangle$.

Since $\Omega_{eff} \ll \kappa$ at large detuning, the write process operates in the rate equation limit. In other words, there is no Rabi flopping between $|A\rangle$ and $|C\rangle$, and write photons simply get injected into the cavity at the constant rate [42]

$$R_{AC} = \frac{\Omega_{eff}^2}{\kappa} = \frac{1}{\kappa}\left(\frac{\sqrt{N_a}\omega_p g_w}{2\delta}\right)^2 \tag{3.14}$$

In fact, there is an even simpler picture describing the rate at which write photons are emitted into the cavity. For small Ω_{eff}, the problem of spontaneous emission reduces to an off-resonant scattering problem. The rate at which write photons are scattered off the write pump beam into free space, in the limit of large δ, is given by [40]:

$$R_{fs} = \frac{1}{\delta^2}\left(\frac{\Gamma}{2}\right)^3 \frac{I}{I_s} \tag{3.15}$$

where I and I_s are the applied and saturation intensities respectively. The rate at which write photons are scattered into the cavity is then enhanced by the collective cooperativity $N_a\eta$:

$$R_{cav} = N_a \eta R_{fs} = \frac{1}{\kappa}\left(\frac{N_a g_w^2}{4\delta^2}\right)\left(\frac{1}{2}\Gamma^2 \frac{I}{I_s}\right) \tag{3.16}$$

Using the relation $2(\omega_p/\Gamma)^2 = I/I_s$, we reconcile the two pictures describing the emission of the write photon: $R_{cav} = R_{AC}$.

3.7 Summary of Write and Read Processes

Many important ideas have been presented in this chapter — cooperativity, superradiance, four-wave mixing, and the three-level system in both the strong coupling and rate equation limits. We reiterate how these concepts fit together in the mechanism for generating correlated photon pairs: initially, all the atoms are optically pumped to $|a\rangle$. One of the collectively coupled atoms off-resonantly scatters a write photon from the write laser beam as it makes a transition from $|a\rangle$ to $|f\rangle$ at a constant rate R_{AC}. Given this constant rate, the emission of the write photon into the cavity initializes two processes: the exponential decay of the write photon out of the cavity, and the read process. For the read process, the emission of the read photon into the cavity mode is enhanced by superradiance (or four-wave mixing, which is equivalent to superradiance in an extended sample), because we are unable to tell which of the atoms had made the $|a\rangle \rightarrow |f\rangle$ transition. The time-dependent probability amplitude for the read photon to be emitted is governed by three-level dynamics, which must be convolved with the exponentially decaying time dependence describing when the emitted write photon leaves the cavity. Such a convolution encodes a strong overlap between the state of the system and the almost-dark state (i.e. very little excited state $|e\rangle$ component) for the read process. Good overlap with the almost-dark state ensures that most of the read photons decay into the cavity mode instead of into free space, which translates into high recovery efficiency of the read photons.

Chapter 4

Generation of Correlated Photon Pairs

4.1 Experimental Setup

Modeling the cavity and collectively coupled cesium atoms as a three-level system has provided us with an understanding of how correlated write and read photon pairs can be generated. We now turn to the practical details of the experiment. This section gives a sketch of the key components of the experimental setup used to generate correlated photon pairs. Technical details of the laser system, optical pumping procedure and magneto-optical trap (MOT) holding the cesium atoms can be found in Adam Black's thesis [6].

Fig. 4-1 shows a schematic diagram of the experimental setup. The cesium atoms are held by a MOT in a low-finesse ($\mathcal{F} = 250$), single-mode cavity, of which $N_a \sim 10^4$ atoms are positioned at the waist ($w_c = 110$ μm) of the TEM_{00} cavity mode. The Rabi splitting due to a single atom coupled to the cavity is given by $2g/2\pi = 0.36$ MHz, and the single atom cooperativity is $\eta = 7.3 \times 10^{-4}$, which translates to a collective cooperativity of $N_a\eta \sim 5$. π-polarized, counter-propagating write and read laser pump beams are applied continuously from the side of the cavity. The read pump beam is derived by retro-reflecting the write pump beam off a mirror, hence

both write and read pump beams operate at the same frequencies and intensities[1]. Photons can either be emitted into free space at a rate of $\Gamma/2\pi = 5.2$ MHz, or out of the cavity at a rate of $\kappa/2\pi = 8.6$ MHz. Because the reflectivities of the two cavity mirrors differ from each other, the σ^--polarized write and σ^+-polarized read photons tend to leak out through the upper cavity mirror into the detection setup.

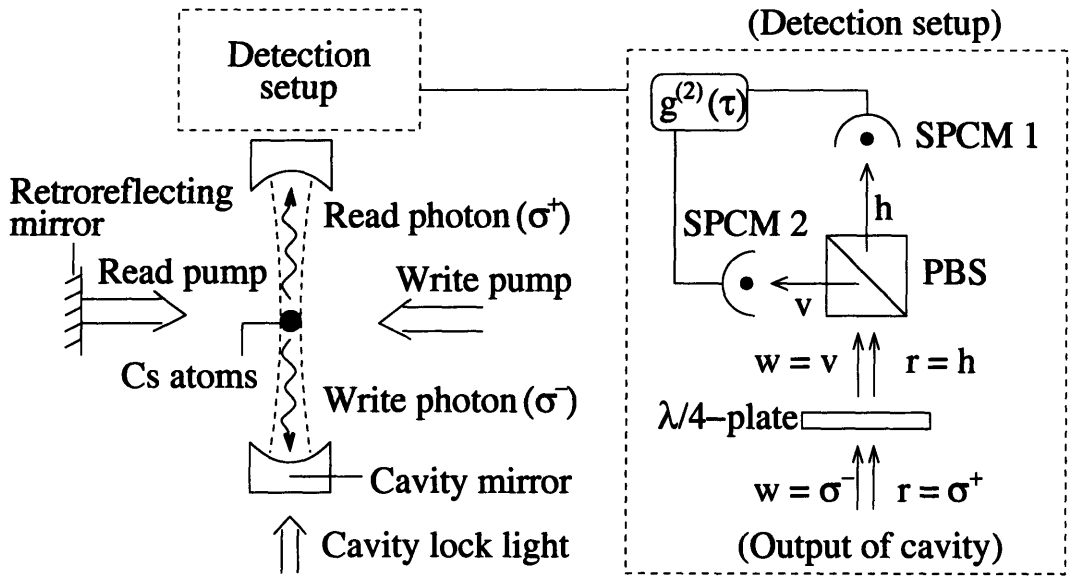

Figure 4-1: Experimental setup for generating correlated photon pairs. The cavity lock light is a grating laser beam sent through the cavity in between sequences of data taking, so as to probe and lock the cavity frequency to atomic resonance. The MOT beams and an additional laser used in optical pumping are not drawn. In the detection setup, "w" and "r" denote write and read photons, while "v" and "h" denote vertical and horizontal polarizations respectively.

Outside of the cavity, a quarter-waveplate transforms the polarizations of the write and read photons into vertical v and horizontal h respectively. The v-polarized write and h-polarized read photons are then separated by a polarizing beam splitter (PBS) to enter their respective fiber-coupled single-photon counting modules (SPCM-AQR-13-FC from Perkin-Elmer), which output TTL pulses to a fast counting card (P7888 from Fast ComTec GmbH) that can detect the arrival time of the photons with ns resolution.

[1]The write pump beam in turn comes from a Distributed Bragg Reflector (DBR) laser diode, whose linewidth has been narrowed by optical feedback from a high-finesse Fabry-Perot cavity [6, 49].

4.2 Photon Statistics

Based on the output of the SPCMs, we can measure the intensity cross correlation $g_{wr}(\tau)$ to characterize how correlated the write and read photons are to each other. The intensity cross correlation measures the joint observation of a write photon at an initial time (which is set to be zero) and a read photon at some later time τ, and compares this joint rate to the rate expected from uncorrelated write and read photon pairs:

$$g_{wr}(\tau) = \frac{\langle N_w(0) N_r(\tau) \rangle}{\langle N_w \rangle \langle N_r \rangle}, \tag{4.1}$$

where $\langle N_w \rangle$, $\langle N_r \rangle$ are the time-averaged rates of the write and read photons. Note that Eq. (4.1) follows from the general expression for the intensity correlation function, defined in terms of photon creation $\hat{a}^\dagger$ and annihilation $\hat{a}$ operators [45]:

$$g_{ij}(\tau) = \frac{\left\langle \hat{a}_i^\dagger(t) \hat{a}_j^\dagger(t+\tau) \hat{a}_j(t+\tau) \hat{a}_i(t) \right\rangle}{\left\langle \hat{a}_i^\dagger(t) \hat{a}_i(t) \right\rangle \left\langle \hat{a}_j^\dagger(t+\tau) \hat{a}_j(t+\tau) \right\rangle}, \tag{4.2}$$

modified to reflect the cross correlation: $\hat{a}_i(t) \rightarrow \hat{a}_w(0)$, $\hat{a}_j(t+\tau) \rightarrow \hat{a}_r(\tau)$ (and similar replacements for $\hat{a}^\dagger$), where $\left[\hat{a}_w, \hat{a}_r^\dagger\right] = 0, \hat{a}_w^\dagger \hat{a}_w = N_w$, and $\hat{a}_r^\dagger \hat{a}_r = N_r$.

We expect to measure $g_{wr}(\tau) > 1$ when the write and read photons are correlated to each other. A high $g_{wr}(\tau)$, however, does not necessarily imply an efficient generation of correlated photon pairs from the atoms-cavity system. For instance, we can classically induce $g_{wr}(\tau) > 1$ by periodically "chopping" at both inputs of the polarizing beam splitter. On the other hand, the effect of chopping the read and write photons would show up as high autocorrelation functions $g_{ww}(\tau), g_{rr}(\tau)$. The relevant quantity for determining the non-classical correlation between write and read photons is therefore the normalized cross correlation

$$G = \frac{g_{wr}^2(\tau)}{g_{rr}(\tau) g_{ww}(\tau)}, \tag{4.3}$$

where $G > 1$, also known as a violation of the Cauchy-Schwartz inequality [50], indicates that the write and read photons are correlated in a non-classical manner.

Operationally, all of the correlation functions are only defined for some time bin of width T. For example, $g_{wr}(\tau)$ is calculated by sorting the output pulses of the two SPCMs into time bins, and then sliding the two series of time bins with respect to each other for various bin offsets τ and seeing when one series (containing the write photon arrival times) overlaps with the other series (containing the read photon arrival times). The autocorrelations can in principle be similarly obtained by sliding the bins of one SPCM with respect to itself. However, each SPCM is unable to detect a second photon within 50 ns of detecting the first photon, rendering it incapable of giving reliable autocorrelations for $T < 50$ ns. To circumvent this problem of dead time, the write (read) photons are sent to a fiber-coupled 50/50 beam splitter, whose outputs are then connected to the two SPCMs (see Fig. 4-2). The cross correlation measured by the two SPCMs in this configuration thus corresponds to the autocorrelation of write (read) photons.

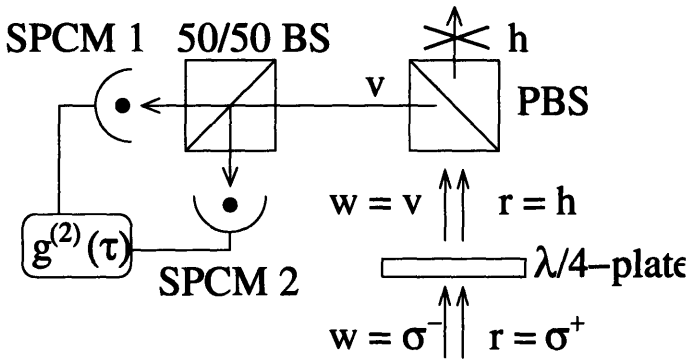

Figure 4-2: Setup for obtaining the write photon autocorrelation, which is equivalent to measuring the cross correlation of the two SPCMs. The read photon output port of the polarizing beam splitter needs to be blocked to prevent reflections back through the cavity and into the write photon output port, which would lead to an artificial increase of the write photon autocorrelation.

4.3 Photon Correlation Results

Fig. 4-3 shows the cross and autocorrelations measured as a function of bin width T for our photon pair source. Since neither the write nor read stream of photons are artificially "chopped" after the cavity, the autocorrelations remain low. Specifically,

the autocorrelations decrease from ~ 2 to 1 as the bin width increases, a characteristic of chaotic light[2] [45]. Combining the low autocorrelations with an initially high g_{wr} (~ 65), we measure a large violation of the Cauchy-Schwartz inequality for small bin widths: the normalized cross correlation is $G = 760^{+2100}_{-320}$ for $T = 60$ ns [4]. Because the read photons are generated on a short time scale of ~ 30 ns, G decreases as the bin width increases and more uncorrelated background photons are included.

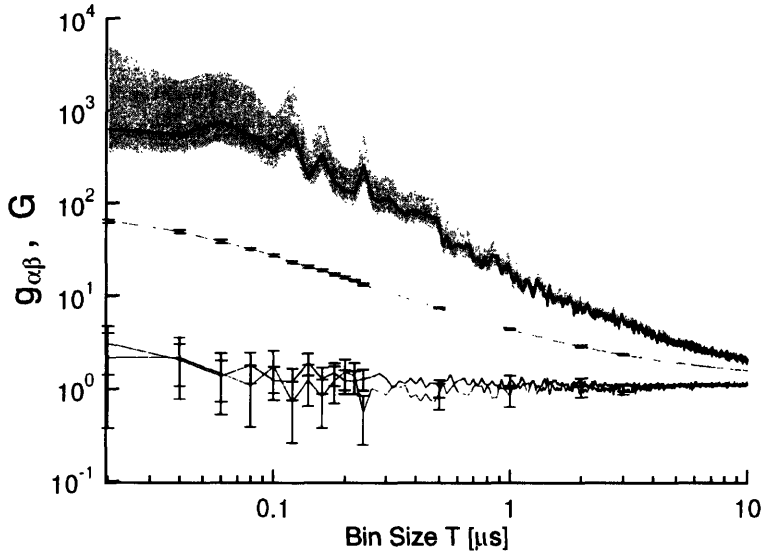

Figure 4-3: Cross and autocorrelations for write and read photons, plotted as a function of bin width T. g_{wr} (green) is combined with g_{ww} (red) and g_{rr} (blue) to yield highly non-classical values for the normalized cross correlation G (black) [4].

The time scale for generating read photons shows up more distinctly in a plot of $g_{wr}(\tau)$ (see Fig. 4-4a). The solid blue curve is a fit to the data, where the curve function is derived from convolving the three-level dynamics of the read process with an exponential decay $e^{-(\kappa/2)\tau}$ of the write photons out of the cavity (see also Fig. 3-7). The presence of Rabi flops indicates that the system is not perfectly projected onto the almost-dark state when the read process is initialized.

Fig. 4-4b shows the cross correlation $g_{hom}(\tau)$ between the write and read photons when the quarter-waveplate is set to convert their respective polarizations into s and

[2]The write (read) photons are considered to be chaotic light, because they are emitted from atoms subject to thermal motion and other broadening mechanisms. This means that one write (read) photon at time 0 can only be correlated with another write (read) photon at time τ if $\tau < \tau_d$, the decoherence time of the atoms. For longer time separations, the two write (read) photons are uncorrelated i.e. the autocorrelation drops to 1.

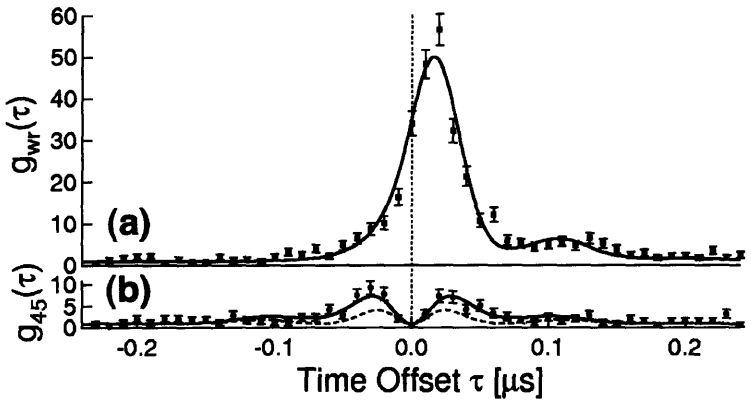

Figure 4-4: (a) Cross correlation between v-polarized write and h-polarized read photons. A finite cross correlation at negative τ simply corresponds to the detection of read photons before the write photons leave the cavity. (b) Cross correlation between s-polarized write and f-polarized read photons, also known as the Hong-Ou-Mandel configuration. The dashed green curve and solid red curves are fits to the data, for write and read photon frequency differences of $\Delta\omega/2\pi = 0$ and $\Delta\omega/2\pi =$ 2.5 MHz respectively [4].

f, which are linear polarizations rotated by 45° away from the vertical and horizontal basis i.e. $s = (v-h)/\sqrt{2}, f = (v+h)/\sqrt{2}$ (see also Fig. 4-5). The arrival of the two photons at the polarizing beam splitter can then be expressed as

$$\begin{aligned}
\hat{s}^\dagger(0)\hat{f}^\dagger(\tau) &= \frac{1}{2}\left(\hat{v}^\dagger(0) - \hat{h}^\dagger(0)\right)\left(\hat{v}^\dagger(\tau) + \hat{h}^\dagger(\tau)\right) \\
&= \frac{1}{2}\left(\hat{v}^\dagger(0)\hat{v}^\dagger(\tau) - \hat{v}^\dagger(0)\hat{h}^\dagger(\tau) + \hat{h}^\dagger(0)\hat{v}^\dagger(\tau) - \hat{h}^\dagger(0)\hat{h}^\dagger(\tau)\right) \\
&= \frac{1}{2}\left(\hat{v}^\dagger(0)\hat{v}^\dagger(0) - \hat{h}^\dagger(0)\hat{h}^\dagger(0)\right), \quad \tau = 0\,. \qquad (4.4)
\end{aligned}$$

where $\hat{s}^\dagger(t), \hat{f}^\dagger(t), \hat{v}^\dagger(t)$ and $\hat{h}^\dagger(t)$ are creation operators for photons polarized along s, f, v and h respectively at time t. Eq. (4.4) shows that a pair of write and read photons will either be simultaneously reflected or transmitted through the polarizing beam splitter, and a coincidence count will *not* be registered between the two SPCMs! The identicalness of the write and read photons at $\tau = 0$ is the explanation for the dip (also known as a Hong-Ou-Mandel dip [51]) in Fig. 4-4b's cross correlation. As τ increases, the write and read photons can be distinguished by their times of arrival at the SPCMs, giving rise to a non-zero cross correlation. The bumps at

$g_{hom}(\pm 30$ ns) are reminiscent of the peak $g_{wr}(30$ ns). In fact, the functional form of $g_{hom}(\tau)$ can be calculated from $g_{wr}(\tau)$. From Eq. (4.4), we understand that the probability amplitudes of the write and read photons destructively interfere at the polarizing beam splitter in the Hong-Ou-Mandel configuration, yielding:

$$\begin{aligned} \tilde{g}_{hom}(\tau) &= \left| \frac{1}{2} \left(\sqrt{\tilde{g}_{wr}(\tau)} e^{i\Delta\omega\tau} - \sqrt{\tilde{g}_{wr}(-\tau)} e^{-i\Delta\omega\tau} \right) \right|^2 \\ &= \frac{1}{4} \left(\tilde{g}_{wr}(\tau) + \tilde{g}_{wr}(-\tau) - 2\sqrt{\tilde{g}_{wr}(\tau)\tilde{g}_{wr}(-\tau)} \cos(2\Delta\omega\tau) \right) , \end{aligned} \quad (4.5)$$

where $\Delta\omega$ is the frequency difference between the write and read photons, and the uncorrelated backgrounds have been subtracted from the correlation functions: $\tilde{g}_{hom}(\tau) = g_{hom}(\tau) - 1$ and $\tilde{g}_{wr}(\tau) = g_{wr}(\tau) - 1$. Eq. (4.5) is plotted in Fig. 4-4b for both $\Delta\omega/2\pi = 0$ and $\Delta\omega/2\pi = 2.5$ MHz. The latter is a better fit to the data, although the frequency difference does not match that predicted from light shifts induced by the π-polarized write and read pump beams.

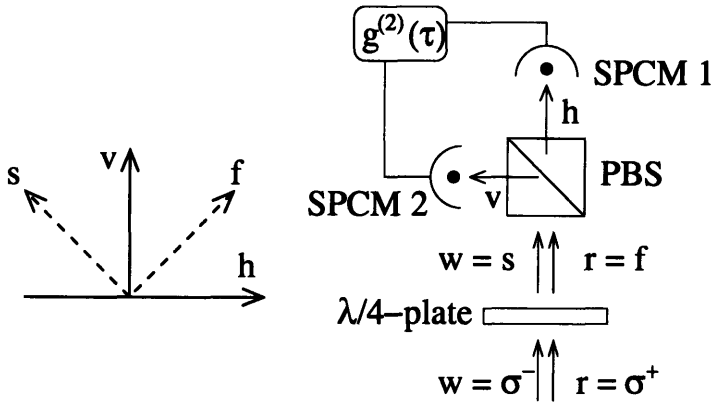

Figure 4-5: Setup for measuring write and read photon cross correlations in the Hong-Ou-Mandel configuration.

We have shown that a cloud of cesium atoms collectively coupled to a low-finesse cavity is capable of generating non-classically correlated pairs of write and read photons. There are many other beautiful results that characterize our photon pair source e.g. high brightness, narrow photon bandwidths and high recovery efficiency of the read photon, which are covered in [4] and shall be left out of this thesis. The purpose of this chapter is to present the relevant correlation results, which provide a back-

ground for discussing two possible applications of the photon pair source: sub-shot noise interferometry and entanglement.

Chapter 5

Towards Sub-Shot Noise Interferometry

5.1 Motivation and Background

Interferometry is an indispensable tool for physicists to probe a wide variety of phenomena, such as Berry's phase [52] and entanglement [53]. A subset of applications, including lithography [54] and gravitational wave detection [55], demands high sensitivity to the phase difference $\Delta\phi$ between two paths of an optical interferometer. Heisenberg's Uncertainty Principle dictates, however, that there is a fundamental limit to the phase sensitivity of an optical interferometer with n photons[1] [56]:

$$\Delta n \Delta\phi \geq \frac{1}{2} \quad \Rightarrow \quad \Delta\phi \sim \frac{1}{\Delta n}, \tag{5.1}$$

The maximum uncertainty in the number of photons Δn is on the order of the number of photons n itself, hence the minimum possible phase uncertainty follows from Heisenberg's Uncertainty Principle:

$$\Delta\phi_{HL} \sim \frac{1}{n}. \tag{5.2}$$

[1] More precisely, the number-phase uncertainty relation is $\Delta n \Delta\phi \geq |1 - 2\pi P(\theta_0)|/2$, where $P(\theta_0)$ is the probability for measuring θ_0, the lowest eigenvalue of the phase operator $\hat{\phi}$. For $P(\theta_0) = 0$, the general uncertainty relation simplifies to Eq. (5.1).

Most interferometry experiments are unable to demonstrate precision at the Heisenberg limit. On the contrary, a typical interferometer, with n photons at input a and no photons at b (see Fig. 5-1), operates at the shot noise limit (also known as the standard quantum limit):

$$\phi_{SNL} = \frac{1}{\sqrt{n}}. \tag{5.3}$$

The shot noise limit can be derived independently of the statistics of the state at input a, e.g. it can be a coherent state or a thermally populated state with average n photons, or a n-photon Fock state. Instead, the limit stems from fluctuations in the vacuum port b, which induce each photon from a to indeterministically traverse the interferometer via either f or s to enter either one of the detectors at d or e. The combined output of the detectors is thus subject to photon shot noise $\sqrt{n}$ [45, 57].

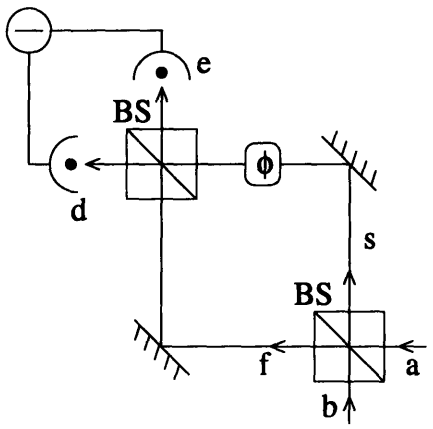

Figure 5-1: Mach-Zehnder interferometer with two 50/50 non-polarizing beam splitters and two mirrors.

To get beyond the shot noise limit, one can leave the state at port a alone (as a coherent/thermal/Fock state) and inject port b with squeezed vacuum, which can be generated via, say, parametric down conversion in an optical cavity [58, 59, 60]. A squeezed state, akin to the coherent state, has minimum uncertainty i.e. $\Delta n \Delta\phi = 1/2$, but its phase uncertainty is "squeezed" to below the shot noise limit: $\Delta\phi = e^{-(r/2)}/\sqrt{n}$, where r is the squeezing parameter. The main difficulty with using squeezed states, however, is that even with a source capable of producing highly squeezed vacuum, any losses in the interferometer couples in additional vacuum fluc-

tuations, which can bring the overall phase sensitivity back to the shot noise limit.

An alternative method for sub-shot noise interferometry is to use Fock states at both inputs, which may [61] or may not [1] be entangled. In particular, Holland and Burnett proposed sending Fock states of equal photon number $|n_{hb}\rangle$ into the two inputs, to achieve a Heisenberg limited phase sensitivity of $1/(2n_{hb})$. One can motivate the high phase sensitivity by considering two classical fields $\{\alpha_{in}e^{i\theta_{in}}, \beta_{in}e^{i\phi_{in}}\}$ incident on a 50/50 beam splitter (see Fig. 5-2). The two output fields then differ in phase and amplitude by [1]:

$$\tan(\phi_{out} - \theta_{out}) = \frac{\alpha_{in} - \beta_{in}}{2\alpha_{in}\beta_{in}\cos(\phi_{in} - \theta_{in})}, \tag{5.4a}$$

$$(\alpha_{out})^2 - (\beta_{out})^2 = 2\alpha_{in}\beta_{in}\sin(\phi_{in} - \theta_{in}) . \tag{5.4b}$$

In other words, two input fields with the same amplitude ($\alpha_{in} = \beta_{in}$) will give rise to two output fields with no phase difference ($\phi_{out} = \theta_{out}$) after the beam splitter, regardless of the input field phases. Quantum mechanically, such a result means that the noise of the phase difference between two paths of an interferometer is minimized to the Heisenberg uncertainty level, when states with precisely equal photon numbers are used at each input [45].

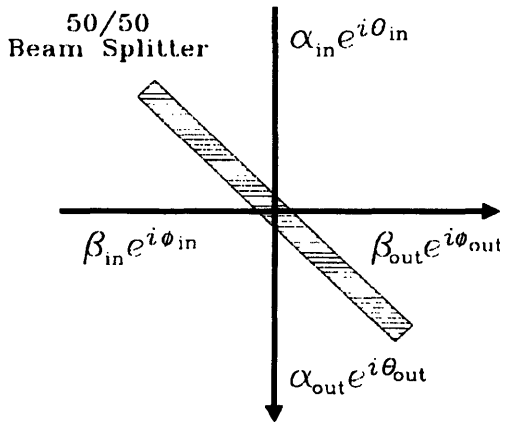

Figure 5-2: Classical input and output electric fields of a 50/50 non-polarizing beam splitter [1].

5.2 Holland-Burnett Scheme with Correlated Photon Pairs

The Holland-Burnett scheme for $n_{hb} = 1$ can be realized with a source of correlated photon pairs, such as the atoms-cavity system described in the previous two chapters. The most direct implementation is depicted in Fig. 5-3a, where the write and read photons, after being split by the polarizing beam splitter (originally part of the detection setup), are sent through two 50/50 beam splitters before being detected by the SPCMs. The path length difference is varied as a piezoelectric stack dithers one of the mirrors back and forth.

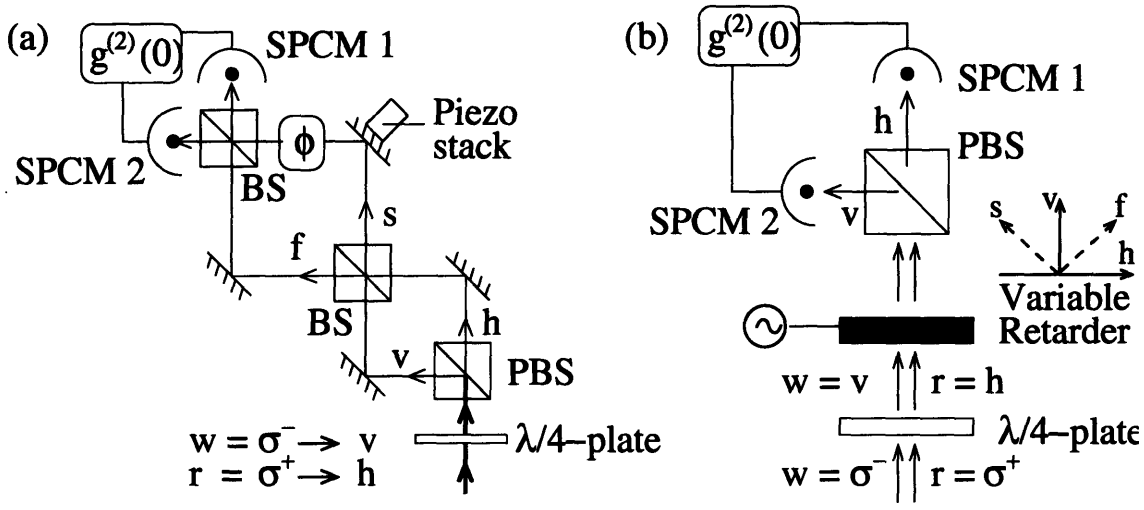

Figure 5-3: Two possible implementations of the Holland-Burnett scheme for $n_{hb} = 1$: (a) Sending the polarization-separated write and read photon pairs through a spatial Mach-Zehnder interferometer, formed by two 50/50 non-polarizing beam splitters and two mirrors; (b) Sending the write and read photons through a variable retarder before polarization-separating them.

On the other hand, Fig. 5-3b offers a technically simpler way of realizing such a Mach-Zehnder interferometer: only a variable liquid crystal retarder (LVR-200-IR2 from Meadowlark Optics), whose retardance changes with the amplitude of an applied 2 kHz AC voltage, needs to be inserted between the quarter-waveplate and polarizing beam splitter of the original detection setup. The quarter-waveplate is set to convert the polarizations of the write and read photons into v and h respectively, while the

retarder is aligned such that its slow s and fast f axes are oriented at 45° away from v and h. Instead of varying the path length difference spatially, the optical path lengths of the photons are now changed, as the variable retarder imparts a phase shift $e^{i\phi}$ to each photon polarized along its slow axis. The following equations illustrate how such a retarder setup maps back to a Holland-Burnett Mach-Zehnder interferometer:

$$\hat{w}^\dagger \hat{r}^\dagger \rightarrow \hat{\sigma}_-^\dagger \hat{\sigma}_+^\dagger \qquad \text{out of cavity} \tag{5.5a}$$

$$\rightarrow \hat{v}^\dagger \hat{h}^\dagger \qquad \text{after quarter-waveplate} \tag{5.5b}$$

$$\rightarrow \left(\frac{\hat{f}^\dagger + \hat{s}^\dagger}{\sqrt{2}}\right)\left(\frac{\hat{f}^\dagger - \hat{s}^\dagger}{\sqrt{2}}\right) \qquad \text{in basis of retarder} \tag{5.5c}$$

$$= \frac{1}{2}\left[(\hat{f}^\dagger)^2 - (\hat{s}^\dagger)^2\right]$$

$$\rightarrow \frac{1}{2}\left[(\hat{f}^\dagger)^2 - (\hat{s}^\dagger)^2 e^{2i\phi}\right] \qquad \text{by action of the retarder} \tag{5.5d}$$

$$\rightarrow \frac{1}{2}\left[\left(\frac{\hat{v}^\dagger + \hat{h}^\dagger}{\sqrt{2}}\right)^2 - \left(\frac{\hat{v}^\dagger - \hat{h}^\dagger}{\sqrt{2}}\right)^2 e^{2i\phi}\right] \qquad \text{in basis of SPCM detectors} \tag{5.5e}$$

$$= \frac{1}{4}\left[\left((\hat{v}^\dagger)^2 + (\hat{h}^\dagger)^2\right)\left(1 - e^{2i\phi}\right) + 2\hat{h}^\dagger \hat{v}^\dagger \left(1 + e^{2i\phi}\right)\right]$$

We are only interested in the coincidence detection[2] of h and v photons. The probability of detecting a coincidence from one write and read photon pair is hence given by the square of the coefficient of the above $\hat{h}^\dagger \hat{v}^\dagger$ term:

$$P_{11}^0 = \left|\frac{1 + e^{2i\phi}}{2}\right|^2 = \frac{1 + \cos 2\phi}{2} \tag{5.6}$$

P_{11}^0 varies as $\cos 2\phi$ instead of as $\cos \phi$, due to the possibility of both photons simultaneously traversing the phase-shifted path s (see Fig. 5-1) — a picture reminiscent of the physics behind the Hong-Ou-Mandel dip discussion from the previous chapter (Fig. 4-4b). For this reason, the fringes from the output coincidence detection are termed "Hong-Ou-Mandel interference fringes".

[2]In Eq. (5.5), we only considered pairs of write and read photons generated at the same time t. If we allowed for time-delayed pairs i.e. $\hat{w}^\dagger(t)\hat{r}^\dagger(t+\tau)$, we would not have been able to cancel out the terms $-\hat{f}^\dagger(t)\hat{s}^\dagger(t+\tau) + \hat{s}^\dagger(t)\hat{f}^\dagger(t+\tau)$ in Eq. (5.5c), which would have prevented an equivalent mapping back to the Holland-Burnett scheme.

For N Poisson-distributed pairs of write and read photons entering the interferometer, the expectation of detecting M coincidences is then

$$\langle M \rangle = \langle N \rangle P_{11}^{0} = \langle N \rangle \frac{1 + \cos 2\phi}{2}, \tag{5.7}$$

assuming perfect detection efficiency. The phase uncertainty should therefore be $\Delta\phi = (1/2)(1/\sqrt{N}) = 1/(2\sqrt{N})$, where the factor of $(1/2)$ comes from Holland's and Burnett's predictions, and $\sqrt{N}$ is the standard deviation of the N independent pairs (a "hand-waving" argument!). Contrasted against the shot noise limit for an interferometer with $2N$ photons i.e. $\Delta\phi_{SNL} = 1/(\sqrt{2N})$, we can see how the $\sqrt{2}$ reduction in the phase uncertainty comes about: $\langle M \rangle$ varies at twice the expected frequency i.e. $\cos 2\phi$, so $|\partial\phi/\partial \langle M \rangle|$ reduces by a factor of 2. However, ΔM increases by $\sqrt{2}$ because there are twice as many photons that can enter the interferometer paths s or f. Using

$$\Delta\phi = \left| \frac{\partial\phi}{\partial \langle M \rangle} \right| \Delta M, \tag{5.8}$$

we achieve an overall reduction of $\sqrt{2}$ in the phase noise when compared to the shot noise limit.

5.3 Conditions for Sub-Shot Noise Interferometry

A more careful analysis of the Holland-Burnett phase uncertainty would take into account factors like uncorrelated background counts, detection efficiencies ($0 \leq \{\alpha_v, \alpha_h\} \leq 1$) and inability of the detectors to distinguish between one and two photons at short time scales $T < 50$ ns. The following calculations of $\Delta\phi$, which take into the above factors, follow closely from those presented by Kuzmich and Mandel [7].

Suppose that for each pair of photons arriving at the interferometer inputs, there is a probability of $1 - \beta$ that the two photons are uncorrelated. Accounting for the detection efficiencies too, the probability of detecting one coincidence from one input

photon pair then becomes

$$P_{11} = \alpha_v \alpha_h \frac{1 + \beta \cos 2\phi}{2} . \tag{5.9}$$

The visibility of the fringes, defined to be $\mathcal{V} \equiv (P_{11}^{max} - P_{11}^{min})/(P_{11}^{max} + P_{11}^{min})$, reduces to β.

Given N photon pairs, the conditional probability $P(M|N)$ for M coincidences is

$$P(M|N) = \binom{N}{M} (P_{11})^M (1 - P_{11})^{N-M} , \quad (M \leq N) . \tag{5.10}$$

The probability of detecting M coincidences over a time period, during which the probability of N photon pairs traversing the interferometer is $P(N)$, is thus

$$p(M) = \sum_{N=M}^{\infty} P(M|N) P(N) . \tag{5.11}$$

To obtain $\Delta M \equiv \langle (\Delta M)^2 \rangle^{1/2} = (\langle M^2 \rangle - \langle M \rangle^2)^{1/2}$, we need to calculate $\langle M \rangle$ and $\langle M^2 \rangle$:

$$\begin{aligned}
\langle M \rangle &= \sum_{M=0}^{\infty} M p(M) \\
&= \sum_{M=0}^{\infty} \sum_{N=M}^{\infty} M \binom{N}{M} (P_{11})^M (1 - P_{11})^{N-M} P(N) \\
&= \sum_{N=0}^{\infty} \sum_{M=0}^{\infty} M \binom{N}{M} (P_{11})^M (1 - P_{11})^{N-M} P(N) \\
&= \sum_{N=0}^{\infty} N P_{11} P(N) \\
&= \langle N \rangle P_{11} ,
\end{aligned} \tag{5.12}$$

from which

$$\left| \frac{\partial \phi}{\partial \langle M \rangle} \right| = \frac{1}{\langle N \rangle \alpha_v \alpha_h \beta \sin 2\phi} , \tag{5.13}$$

where we have substituted Eq. (5.9) for P_{11}. Additionally,

$$\begin{aligned} \langle M^2 \rangle &= \sum_{M=0}^{\infty} M^2 p(M) \\ &= \langle N \rangle P_{11}(1 - P_{11}) + \langle N^2 \rangle (P_{11})^2 . \end{aligned} \tag{5.14}$$

Therefore the uncertainty in the number of coincidences detected is

$$\begin{aligned} \Delta M &= \left[\langle M^2 \rangle - \langle M \rangle^2 \right]^{1/2} \\ &= \left[\langle N \rangle P_{11}(1 - P_{11}) + \langle (\Delta N)^2 \rangle (P_{11})^2 \right]^{1/2} . \end{aligned} \tag{5.15}$$

For the case of perfect correlation between photon pairs $\beta = 1$, perfect detection efficiencies $\{\alpha_v, \alpha_h\} = 1$, and perfect detector ability to distinguish between one and two photons $\langle (\Delta N)^2 \rangle = 0$, the uncertainty in the number of coincidences detected becomes

$$\Delta M = \frac{\sqrt{\langle N \rangle}}{2} \sin 2\phi . \tag{5.16}$$

Using Eq. (5.8), the phase uncertainty reduces to the same expression obtained from the previous hand-waving argument:

$$\Delta \phi = \frac{1}{2\sqrt{N}} . \tag{5.17}$$

On the other hand, taking into account all three imperfections yields

$$\Delta M = \left[\langle N \rangle \alpha_v \alpha_h \frac{1 + \beta \cos 2\phi}{2} \right]^{1/2} \tag{5.18}$$

where imperfect detector ability to distinguish between one and two photons results in $\langle (\Delta N)^2 \rangle = \langle N \rangle$ for the Poisson-distributed pairs. The phase uncertainty is then given by

$$\Delta \phi = \frac{1}{\beta \sin 2\phi} \left(\frac{1 + \beta \cos 2\phi}{2 \langle N \rangle \alpha_v \alpha_h} \right)^{1/2} . \tag{5.19}$$

Compared to the shot noise limit of an imperfect system

$$\Delta\phi_{SNL} = \frac{1}{\sqrt{2\langle M(\phi=0)\rangle}} = \frac{1}{\sqrt{(1+\beta)\langle N\rangle \alpha_v \alpha_h}}, \tag{5.20}$$

the phase uncertainty of the Holland-Burnett interferometer needs to have some minimum fringe visibility β_0 to demonstrate sub-shot noise interferometry:

$$\frac{\Delta\phi}{\Delta\phi_{SNL}} = \left[\frac{(1+\beta)(1+\beta\cos 2\phi)}{2\beta^2 \sin^2 2\phi}\right]^{1/2} \quad (\text{demand} \leq 1 \text{ for some } \phi). \tag{5.21}$$

Fig. 5-4 plots the above ratio of phase uncertainties for various values of β, which also represents the fraction of correlated pairs. It turns out that $\beta \geq \beta_0 = 0.843$ is needed for $\Delta\phi$ to get below the shot noise limit.

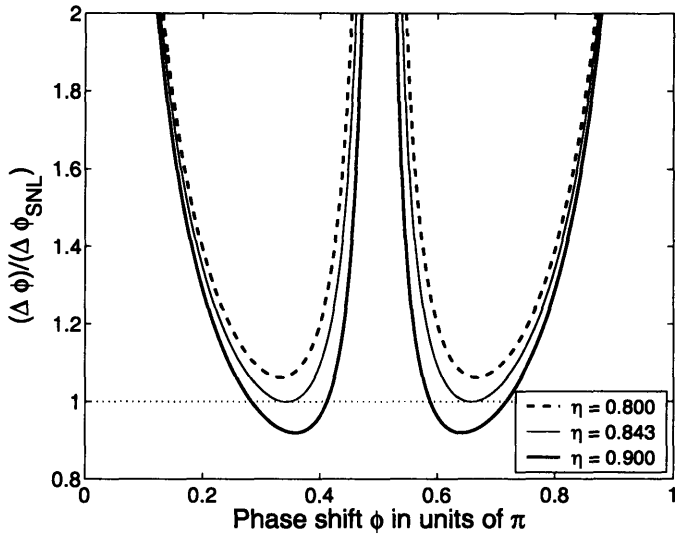

Figure 5-4: Ratio of phase uncertainties, plotted as a function of phase for various fringe visibilities β. The ratio diverges at $\phi = \pi/2$ for all $\beta < 1$.

Kuzmich and Mandel have also made the important observation that the ratio of phase uncertainties does not depend on the detection efficiencies [7]. The lack of dependence is due to the nature of the detection setup: putting in $\langle N\rangle$ photon pairs with detection efficiencies α_v, α_h is equivalent to putting in $\langle N\alpha_v\alpha_h\rangle$ photon pairs with perfect detection efficiencies.

5.4 Observation of Biphoton Interference Fringes

We return to the actual interference experiment performed with our correlated photon pairs. Before observing the interference fringes, we calibrate the interferometer phase in situ, as a function of the amplitude of AC voltage applied to the variable retarder. For the calibration, cavity lock light is sent through an empty cavity and onto the setup in Fig. 5-3, with one of the output ports of the polarizing beam splitter blocked and the other output port connected to an avalanche photodiode instead of a SPCM. Fig. 5-5a shows the avalanche photodiode output signal as the applied voltage amplitude is slowly dithered. The phase can be then backed out from the avalanche photodiode signal V_{APD}(see Fig. 5-5b):

$$V_{APD} = V_0 \frac{1 + \cos\phi}{2}, \tag{5.22}$$

where V_0 is the avalanche photodiode signal with no phase shift imparted.

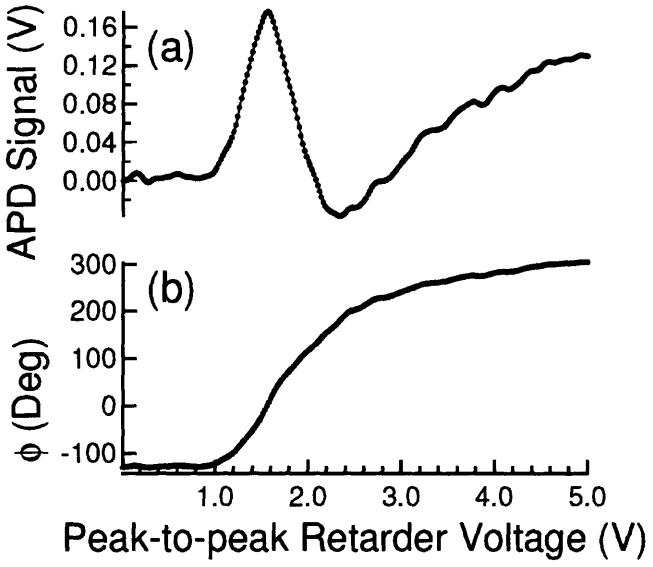

Figure 5-5: (a) Voltage output of avalanche photodiode during a scan of the variable retarder voltage. (b) Calibration of phase imparted by the variable retarder versus applied voltage.

Equipped with the phase calibration, we observe the Hong-Ou-Mandel interference fringes using the following procedure: the correlated photon pairs are generated as

described in Chapter 4, and then sent through the detection/interferometry setup shown in Fig. 5-3b. For a fixed retarder voltage corresponding to some phase shift, the cross correlation data is collected by the two SPCMs and averaged for 45 minutes. Because we only consider photon pairs that arrive at the same time (see also the second footnote of this chapter), only $g_{wr}(\tau = 0)$, analyzed for a bin width of 5 ns, is registered as one data point on the interference fringe curve. To observe the full interference fringe curve, the above steps are repeated for different retarder voltages.

Fig. 5-6 shows the final Hong-Ou-Mandel interference fringes, measured over two full cycles. The first feature to note is that the fringes vary as $\cos 2\phi$ instead of $\cos \phi$, as expected from Section 5.3's analysis of biphoton interference. The second feature is the fringe visibility, which is measured to be $\beta = 0.84 \pm 0.04$ by fitting the data to Eq. (5.12). Since $\beta \sim \beta_0$, we have not yet demonstrated sub-shot noise interferometry with our correlated photon pairs. Nevertheless, there exists the potential to achieve sub-shot noise interferometry, by tuning up the system to obtain a higher fraction of correlated photon pairs.

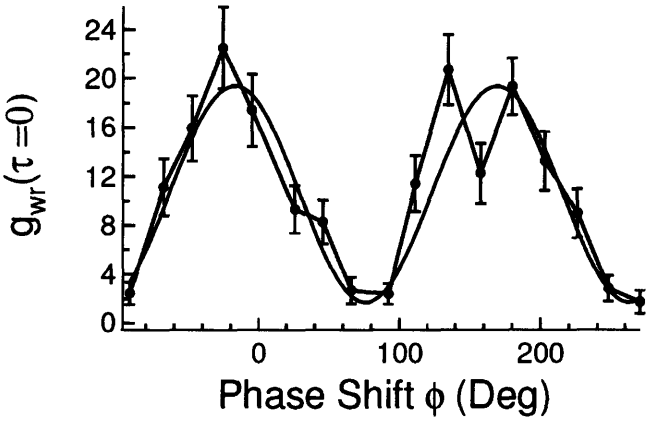

Figure 5-6: Hong-Ou-Mandel interference fringes, measured using the variable retarder setup. The red curve is a fit of the data to $g_{wr} = \alpha(1 + \beta\cos(\gamma\phi + \epsilon))/2$, yielding a periodicity of $\gamma = 1.93 \pm 0.04$ and fringe visibility $\beta = 0.84 \pm 0.04$.

The next natural step for us to take is to tune up our atoms-cavity system to obtain a higher fraction of correlated photon pairs, which would directly translate to a larger fringe visibility β. Afterall, the maximum value of $g_{wr}(\tau = 0)$ in Fig. 5-6 is only 22, and we have observed higher cross correlations in Chapter 4. On the other

hand, even if we could claim sub-shot noise interferometry then, the result would not be new: physicists have performed similar experiments with parametric down converted pairs before [7]! The true purpose of this biphoton interference experiment is to check that our photon pair source may be used for at least the same applications as existing parametric down converters. In this chapter, we have shown steps towards achieving sub-shot noise interferometry. In the following chapter, we shall turn to a second application that, to the best of our knowledge, is novel: polarization-time entanglement of photons.

Chapter 6

Polarization-Time Entanglement of Photons

6.1 Definition of an Entangled State

Entangled states form the cornerstone of many "quantum applications": quantum cryptography [9], quantum teleportation [62], quantum computation [63]... the list goes on. Given the importance of entangled states in today's quest towards quantum information technology, it is crucial to understand what it means for a state to be entangled: *An entangled state is a state that cannot be expressed as a product state* [64].

The simplest examples of entangled states are given by the Bell states

$$\frac{1}{\sqrt{2}}\left(|A_1A_2\rangle \pm |B_1B_2\rangle\right) , \quad \frac{1}{\sqrt{2}}\left(|A_1B_2\rangle \pm |B_1A_2\rangle\right) , \tag{6.1}$$

which express entanglement between two systems, each of which may possess attribute A or B. The subscripts "1" and "2" indicate two modes that each system can be in. For instance, we can entangle the polarizations (V or H) of two photons that may enter two different spatial modes (k_1 or k_2):

$$\frac{1}{\sqrt{2}}\left(|V_{k_1}V_{k_2}\rangle \pm |H_{k_1}H_{k_2}\rangle\right) , \quad \frac{1}{\sqrt{2}}\left(|V_{k_1}H_{k_2}\rangle \pm |H_{k_1}V_{k_2}\rangle\right) . \tag{6.2}$$

The above states can be produced from a type-II parametric down converter (see Fig. 6-1) [5].

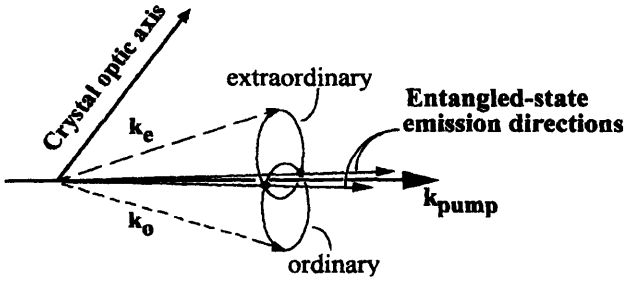

Figure 6-1: "Extraordinary" and "ordinary" photons (i.e. h- and v-polarized photons) are emitted into two separate cones $\vec{k}_e$ and $\vec{k}_o$ during type-II parametric down conversion. Photons traversing along the points of intersection between the two cones are entangled [5].

Before the advent of the type-II parametric down converter, most physicists generated "entanglement" only upon post-selection. One popular method was to send a pair of v- and h-polarized photons to the two input modes $\{a, b\}$ of a non-polarizing beam splitter, and then post-selecting for coincidences between the two output port modes $\{1, 2\}$ [65]:

$$\begin{aligned} |H_a V_b\rangle &= \frac{1}{\sqrt{2}} |H_1 + iH_2\rangle \otimes \frac{1}{\sqrt{2}} |-iV_1 + V_2\rangle \\ &= \frac{1}{2}(|H_1V_2\rangle + |V_1H_2\rangle - i\,|H_1V_1\rangle + i\,|H_2V_2\rangle) \qquad (6.3) \\ &\rightarrow \frac{1}{\sqrt{2}}(|H_1V_2\rangle + |V_1H_2\rangle) \quad \text{upon post-selection} \qquad (6.4) \end{aligned}$$

Note that despite Eq. (6.4)'s similarity to one of the Bell states, the system is *not fundamentally entangled*, since it started out as a product state.

Similarly, the state we generated with our write and read photons in the Hong-Ou-Mandel configuration from Chapter 4 is not an entangled state, despite its resemblance

to a Bell state upon coincidence detection (see also Eq. (4.4)):

$$\begin{aligned} |S_t F_{t'}\rangle &= \frac{1}{\sqrt{2}}|V_t - H_t\rangle \otimes \frac{1}{\sqrt{2}}|V_{t'} + H_{t'}\rangle \\ &\rightarrow \frac{1}{\sqrt{2}}(|V_t V_t\rangle - |H_{t'} H_{t'}\rangle), \quad t = t'. \end{aligned} \tag{6.5}$$

How then can one create an entangled state with our new photon pair source? Up to this point, we have only used atoms starting in $|F = 3, m_F = -3\rangle$ to generate σ^--polarized write and σ^+-polarized read photons. If one could also initialize atoms in $|F = 3, m_F = -3\rangle$, one could additionally produce σ^+-polarized write and σ^--polarized read photons (see Fig. 6-2):

$$\begin{aligned} |\Psi\rangle &= \frac{1}{\sqrt{2}}(|\sigma_t^- \sigma_{t'}^+\rangle + e^{i\theta}|\sigma_t^+ \sigma_{t'}^-\rangle) \\ &\rightarrow \frac{1}{\sqrt{2}}(|V_t H_{t'}\rangle + e^{i\theta}|H_t V_{t'}\rangle), \quad \text{after quarter-waveplate}, \end{aligned} \tag{6.6}$$

where t and $t' = t + \tau$ are the times at which write and read photons are generated respectively. For $|\Psi\rangle$ to describe a novel polarization-time entangled state, *created without any post-selection*, $e^{i\theta}$ needs to remain as a fixed phase. In fact, from Clebsch-Gordan coefficients, we predict $e^{i\theta} = 1$. However, if $e^{i\theta}$ varies from one optical pumping cycle to the other, we would only obtain a statistical mixture of $|\sigma_t^- \sigma_{t'}^+\rangle$ and $|\sigma_t^+ \sigma_{t'}^-\rangle$ photon pairs.

6.2 Generation of Entangled Photons

To initialize atoms in both $|F = 3, m_F = \pm 3\rangle$ states, one needs to change the optical pumping procedure. We remind the reader of the convention that the quantum number F refers to the ground state $6^2S_{1/2}$, while F' refers to the excited state $6^2P_{3/2}$. In the original optical pumping scheme, the atoms are cooled by MOT lasers tuned to the $(F =)4 \rightarrow 5'$ cycling transition. For the generation of photon pairs, an additional laser $L_{4\sigma^-}$ that is σ^--polarized and on $(F =)4 \rightarrow 4'$ atomic resonance allows atoms to fall from $|F = 4\rangle$ to $|F = 3\rangle$, from which they can interact with the π-polarized

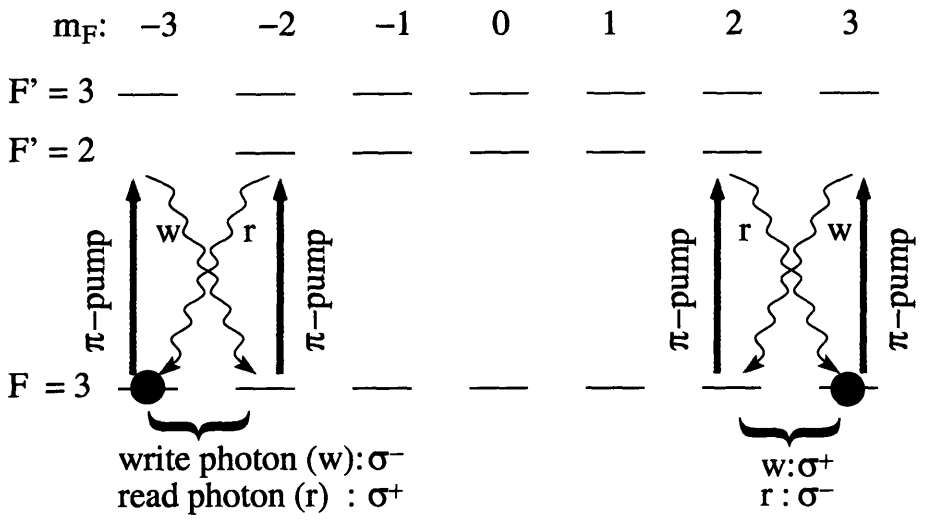

Figure 6-2: Atomic levels used in generating entangled photon pairs.

$(F =)3 \rightarrow 2'$ write and read pump beams. While the atoms would have been pumped to both $|F = 3, m_F = \pm 3\rangle$ by action of the write and read lasers, the σ^--polarization of $L_{4\sigma^-}$ causes atoms to be preferentially pumped to the $|F = 3, m_F = -3\rangle$ dark state.

For the new optical pumping procedure, the write and read beams maintain the same polarization and frequency, while $L_{4\sigma^-}$ is turned off. Atoms can therefore be pumped to both $|F = 3, m_F = \pm 3\rangle$ dark states. To ensure that atoms fall from $|F = 4\rangle$ into $|F = 3\rangle$ in the first place, the MOT lasers are tuned to $(F =)4 \rightarrow 4'$. The rest of the experimental setup remains the same as that depicted in Fig. 4-1. To see if the new optical pumping scheme successfully generates entangled photon pairs, we need to examine the cross correlation function $g_{wr,\Psi}(\tau)$.

Naively, one would expect $g_{wr,\Psi}(\tau)$ to be that of a normal σ^--write and σ^+-read photon pair (Fig. 4-4a), plus its reflection about the vertical axis, because atoms initialized in $|F = 3, m_F = +3\rangle$ now produce σ^+-write photons before σ^--read photons. In partial agreement with these predictions, Fig. 6-3a shows that the cross correlation measured with the new optical pumping scheme is roughly symmetric about the vertical axis. Furthermore, the Rabi flops from Fig. 4-4a also show up in Fig. 6-3a. Surprisingly, however, there is a peak at $\tau = 0$. Qualitatively, we can attribute the central peak to the following mechanism: a σ^--write photon scattered by an atom in $|F = 3, m_F = -3\rangle$ initializes the $m_F = -2$ read process in the same way as before.

However, the scattered σ^--write photon can be reabsorbed on the read process at the $m_F = +3$ end. On average, the reabsorbed photon is only emitted into the cavity one Rabi cycle later, which is also the time taken to generate a σ^+-read photon from the original $m_F = -2$ read process. Therefore, both the σ^- and σ^+ photons appear at the same time, leading to a large cross correlation at $\tau = 0$.

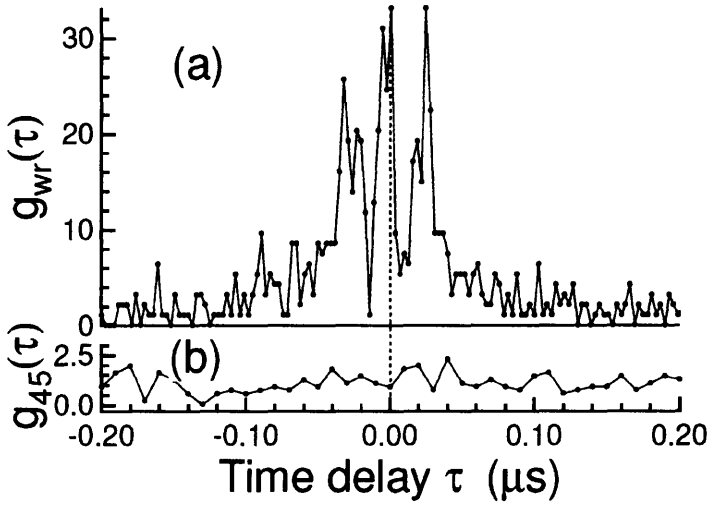

Figure 6-3: Cross correlations between write and read photons generated using the new optical pumping scheme. The photon polarizations have been converted to (a) h and v, or (b) s and f, by the quarter-waveplate. The flatness of $g_{hom,\Psi}(\tau)$ in (b) indicates that the photon pairs are entangled.

How about the cross correlation in the Hong-Ou-Mandel configuration? Here, the measurements present a huge surprise: $g_{hom,\Psi}(\tau)$ is constant at ≈ 1 for all τ, as shown in Fig. 6-3b! The flatness of $g_{hom,\Psi}(\tau)$ indicates that we have entangled photons, instead of a mere statistical mixture. Recall that for the correlated photon pair $|S_t F_{t'}\rangle$ (where s, f are 45° away from v, h),

$$\begin{aligned} \tilde{g}_{hom}(\tau) &= g_{hom}(\tau) - 1 \\ &= \left| \frac{1}{2} \left(\sqrt{\tilde{g}_{wr}(\tau)} e^{i\Delta\omega\tau} - \sqrt{\tilde{g}_{wr}(-\tau)} e^{-i\Delta\omega\tau} \right) \right|^2 . \end{aligned} \tag{6.7}$$

By symmetry, $|F_t S_{t'}\rangle$ would give rise to $\tilde{g}_{hom}(-\tau) = g_{hom}(-\tau) - 1$ in the Hong-Ou-

Mandel configuration. Therefore, for the entangled state $|\Psi\rangle = (|S_t F_{t'}\rangle + |F_t S_{t'}\rangle)/\sqrt{2}$,

$$\begin{aligned}
\tilde{g}_{hom,\Psi}(\tau) &= g_{hom,\Psi}(\tau) - 1 \\
&= \left| \frac{1}{2} \left(\sqrt{\tilde{g}_{hom}(\tau)} + \sqrt{\tilde{g}_{hom}(-\tau)} \right) \right|^2 \\
&= 0 .
\end{aligned} \tag{6.8}$$

Conversely, if we had a statistical mixture of $|S_t F_{t'}\rangle$ and $|F_t S_{t'}\rangle$, we would get a τ-dependent correlation function:

$$\begin{aligned}
\tilde{g}_{hom,\Psi}(\tau) &= \left\langle \left| \frac{1}{2} \left(\sqrt{\tilde{g}_{hom}(\tau)} + e^{i\theta} \sqrt{\tilde{g}_{hom}(-\tau)} \right) \right|^2 \right\rangle_\theta \\
&= \frac{1}{2\pi} \int_0^{2\pi} d\theta \left| \frac{1}{2} \left(1 - e^{i\theta} \right) \right|^2 \tilde{g}_{hom}(\tau) \\
&= \frac{\tilde{g}_{hom}(\tau)}{2}
\end{aligned} \tag{6.9}$$

In fact, there is an even simpler picture for explaining the time independence of $g_{hom,\Psi}(\tau)$:

$$\begin{aligned}
& \hat{s}^\dagger(t)\hat{f}^\dagger(t') + \hat{f}^\dagger(t)\hat{s}^\dagger(t') \\
= \; & \frac{1}{2} \left[\left(\hat{v}^\dagger(t) - \hat{h}^\dagger(t) \right) \left(\hat{v}^\dagger(t') + \hat{h}^\dagger(t') \right) + \left(\hat{v}^\dagger(t) + \hat{h}^\dagger(t) \right) \left(\hat{v}^\dagger(t') - \hat{h}^\dagger(t') \right) \right] \\
= \; & \frac{1}{2} \left[\hat{v}^\dagger(t)\hat{v}^\dagger(t') - \hat{h}^\dagger(t)\hat{h}^\dagger(t') \right] \quad \text{for all } t, t' .
\end{aligned} \tag{6.10}$$

In other words, an entangled pair of write and read photons arriving at the polarizing beam splitter in the Hong-Ou-Mandel configuration will *always* be reflected or transmitted as a pair, regardless of their arrival times!

6.3 Interference of Entangled Photons

We have just shown that polarization-time entangled photon pairs, when polarized in the s, f basis, can destructively interfere at a polarizing beam splitter at all times. To further investigate how these entangled photon pairs interfere, we repeat the Holland-

Burnett interference experiment with the variable retarder setup from Fig 5-3.

Fig. 6-4 shows the entangled state Hong-Ou-Mandel interference fringes, which demonstrates the expected $\cos 2\phi$ variation. Each data point in Fig. 6-4 corresponds to $g_{wr,\Psi}(\tau = 0)$, analyzed for a much larger bin width i.e. 100 ns. One can afford to use larger bin widths for analysis, because the entangled photons interfere at all times. For the same duration of data acquisition, the measured cross correlation yields a lower error bar when analyzed for a larger bin size. The advantage of using entangled photons for interferometry then becomes clear: one only needs $\approx$ 10 minutes per data point to accumulate reasonably good statistics, compared to the previous scheme with 45 minutes per data point! The shortened data collection time, however, comes at the expense of fringe visibility. Recall that from Fig. 4-3, the cross correlation falls with larger bin sizes. Therefore, the peak value in Fig. 6-4 drops to 9, yielding a fringe visibility of $\beta_\Psi = 0.77 \pm 0.03$.

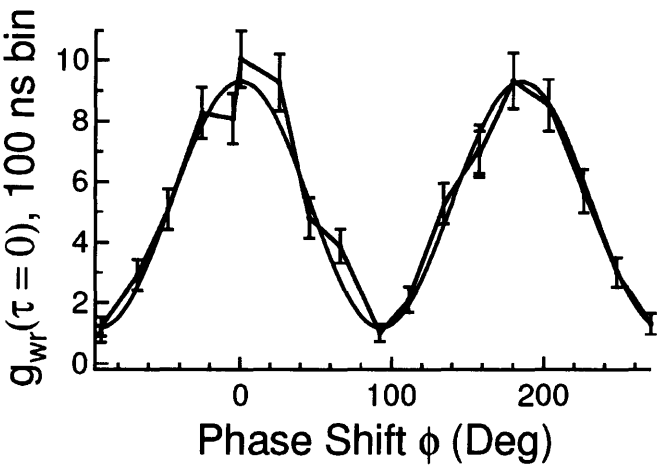

Figure 6-4: Hong-Ou-Mandel interference fringes, obtained by analyzing $g_{wr}(\tau = 0)$ in 100 ns bins for different retarder phase shifts. The red curve, which is a fit to the data, has periodicity $\gamma_\Psi = 1.94 \pm 0.01$ and fringe visibility $\beta_\Psi = 0.77 \pm 0.03$.

The above fringe visibility is lower than that measured with non-entangled pairs, i.e. $\beta = 0.84 \pm 0.04$. Does this comparison then mean that entangled photon pairs are inferior to non-entangled ones with regard to their potential for sub-shot noise interferometry? No. β_Ψ is lower because bins of larger widths are used in the analysis. If the interference fringes are to be remeasured with each data point analyzed in 5 ns

bins, the entangled system may possibly yield a better fringe visibility, since there is a peak in $g_{wr,\Psi}(\tau)$ at $\tau = 0$.

The chief advantage to using entangled photon pairs, however, is not to perform sub-shot noise interferometry. As mentioned at the start of this chapter, entanglement serves as a resource for quantum information technology. The higher the degree of entanglement, the better the system is suited for such quantum applications. To examine the degree to which the write and read photons are polarization-time entangled, we reanalyze the cross correlations for a bin width of 20 ns, and plot $g_{wr,\Psi}(\tau = -30 \text{ ns})$ and $g_{wr,\Psi}(\tau = 20 \text{ ns})$ as functions of retarder phase shift ϕ to obtain two more Hong-Ou-Mandel interference fringe curves (see Fig. 6-5). The bin offsets τ and 20 ns bin width are chosen to focus on the two side peaks from $g_{wr,\Psi}(\tau)$. If all the pairs arriving at the detectors are perfectly entangled, both interference fringe curves will be strictly described in terms of $\cos 2\phi$. Fig. 6-5, however, shows that the fringes are asymmetric i.e. they can be described by an additional $\cos\phi$ term, indicating that the photons are not maximally entangled.

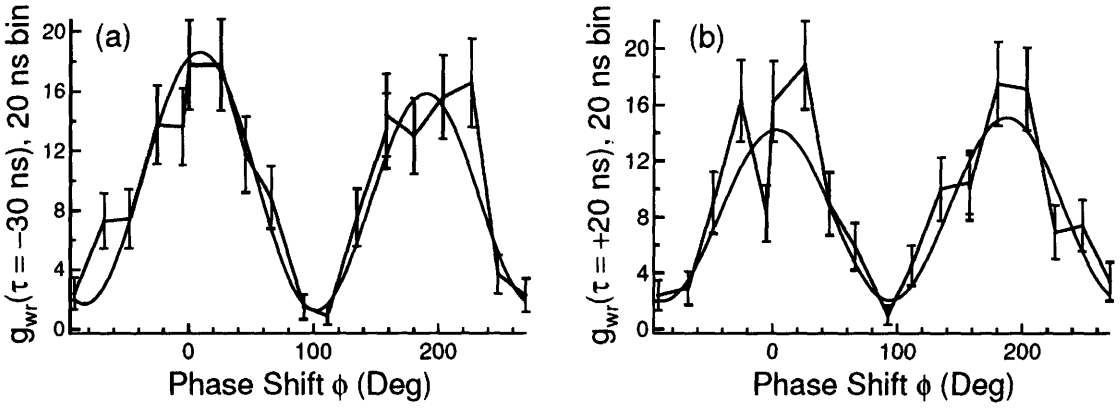

Figure 6-5: Hong-Ou-Mandel interference fringes, obtained by analyzing (a) $g_{wr,\Psi}(\tau = -30 \text{ ns})$ and (b) $g_{wr,\Psi}(\tau = 20 \text{ ns})$ in 20 ns bins. Since neither fringe is symmetric about $\phi \approx 90°$, the photons are not maximally entangled.

6.4 Violation of Bell's Inequality

The most common test for entanglement is to subject the system to an Einstein-Podolsky-Rosen (EPR) experiment, and see if the results violate Bell's inequality. Before applying the EPR experiment to the polarization-time entangled photons, we provide a brief introduction the EPR argument and Bell's inequality. We refer the curious reader to any standard quantum mechanics textbook (for instance, [66]) for further details.

6.4.1 Background of EPR Paradox and Bell's resolution

Since the inception of quantum mechanics in the early 1900s, many physicists struggled with its interpretation. In particular, Einstein, Podolsky and Rosen were among a group of physicists who thought quantum mechanics to be an incomplete theory, i.e. some attributes of a system will always remain hidden from $|\Psi\rangle$, the quantum-mechanical description of the system. To support their interpretation of quantum mechanics, these three physicists proposed the following EPR paradox [67].

Consider the decay of a neutral pion π^0 of spin 0, initially at rest, into an electron e^- and a positron e^+, which fly off in opposite directions (see Fig. 6-6). To conserve angular momentum, the electron and positron possess opposite spins, hence the pair is described by the entangled state

$$|\Psi_{EPR}\rangle = \frac{1}{\sqrt{2}}\left(|\uparrow_+\downarrow_-\rangle - |\downarrow_+\uparrow_-\rangle\right) . \tag{6.11}$$

In a *gedankenexperiment*, one can allow the electron-positron pair to travel until they reach their respective spin-measuring detectors spaced a light year apart from each other. Quantum mechanics dictates that if detector D_+ measures spin up for the positron, the other detector D_- will instantaneously measure spin down for the electron, and vice versa. The "orthodox" interpretation is that the particles were in a superposition of both spin up and spin down during their time-of-flight travel, and the measurement process "collapsed" the overall state into either $|\uparrow_+\downarrow_-\rangle$ or $|\downarrow_+\uparrow_-\rangle$.

However, Einstein, Podolsky and Rosen took the instantaneous correlation between the two detector outputs to mean that detector D_+ needed to send information about its measurement result to D_- at a speed faster than that of light, which was impossible according to special relativity. They therefore concluded that the spins of the two particles must have been pre-determined and described by some variable hidden to quantum mechanics.

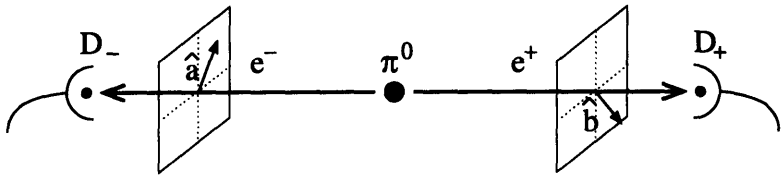

Figure 6-6: Pion decay in an EPR *gedankenexperiment.* $\hat{a}$ and $\hat{b}$ are unit vectors along which the two detectors may be aligned.

The resolution to the two conflicting interpretations was offered by Bell in 1964, who showed that the following inequality must be obeyed if any hidden variables exist [66]:

$$\left|P(\hat{a},\hat{b}) - P(\hat{a},\hat{c})\right| \leq 1 + P(\hat{b},\hat{c})\,, \tag{6.12}$$

where $\hat{a},\hat{b},\hat{c}$ are unit vectors pointing in arbitrary directions. $P(\hat{i},\hat{j})$ is the product of the two detector outputs (with D_+ aligned along $\hat{i}$ and D_- aligned along $\hat{j}$), averaged for all measurements. Clauser, Horne, Shimony and Holt (CHSH) later generalized Bell's inequality [68]:

$$S = |E(\alpha,\beta) - E(\alpha',\beta)| + |E(\alpha',\beta') + E(\alpha,\beta')| \leq 2\,, \quad \text{where} \tag{6.13a}$$

$$E(\alpha,\beta) = \frac{C(\alpha,\beta) + C(\alpha^\perp,\beta^\perp) - C(\alpha^\perp,\beta) - C(\alpha,\beta^\perp)}{C(\alpha,\beta) + C(\alpha^\perp,\beta^\perp) + C(\alpha^\perp,\beta) + C(\alpha,\beta^\perp)}\,. \tag{6.13b}$$

$C(\alpha,\beta)$ is the coincidence between two detectors aligned at angles α and β away from the horizontal axis, and $\alpha^\perp = \alpha + 90°, \beta^\perp = \beta + 90°$. To measure a maximum violation of the CHSH inequality (i.e. $S = 2\sqrt{2}$), one needs to choose $\{\alpha = 0°, \beta = 22.5°\}$ and $\{\alpha' = 45°, \beta' = 67.5°\}$.

Since the 1960s, many physicists have demonstrated a violation of the CHSH form of Bell's inequality, eliminating the "hidden variables" interpretation of quantum

mechanics (reference [69], for instance, illustrates the pioneering work conducted by Aspect, Grangier and Roger). Today, experimental work continues to be performed in this direction, but the focus has changed: the violation of Bell's inequality is now used as an indicator of entanglement in the system [70]. It is with this purpose of entanglement verification that we propose an implementation of the EPR experiment for the write and read photon pairs.

6.4.2 Proposed Implementation of EPR Experiment

Fig. 6-7 shows the experimental setup for a proposed implementation of the EPR experiment. The idea is to split the incident write and read photons in an indistinguishable manner at the 50/50 non-polarizing beam splitter. The polarizing beam splitter and half-waveplate in each output path then serve the purpose of rotating the measurement basis of the SPCM into some angle α or β. Since we would like to verify polarization-*time* entanglement, $E(\alpha, \beta)$ will be formulated in terms of cross correlation functions $g_{\alpha\beta}$ offset from $\tau = 0$, instead of coincidences $C(\alpha, \beta)$ from Eq. (6.13b).

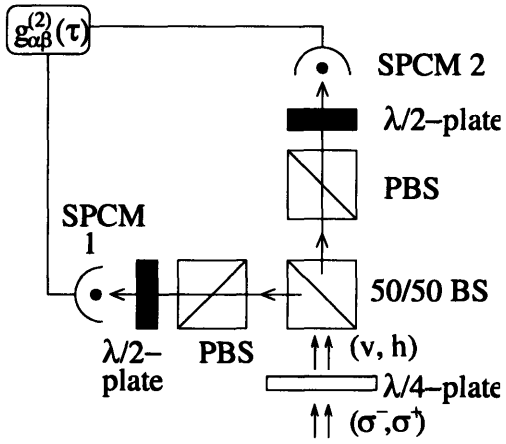

Figure 6-7: Setup for proposed implementation of the EPR experiment.

Although we did not attempt to perform an EPR experiment, we can obtain a quantitative estimate of how much we expect the CHSH inequality to be violated, based on the Hong-Ou-Mandel interference fringes measured in Fig. 6-5. An outline of the calculation is provided below, while the details are given in Appendix A.

The photon pairs after the quarter-waveplate can be most generally described in terms of the probability amplitude $Q(t_0)$ for a pair to arrive at the polarizing beam splitter at time offset t_0, and the probability amplitudes $q(\tau), \ell(\tau)$ and $\rho(\tau)$ that parameterize how likely photons within a given write-read, write-write or read-read pair are spaced by time τ:

$$\begin{aligned} |\psi\rangle \;=\; & \int dt_0' Q(t_0') \int d\tau' \Big\{ \, q(\tau')\, \hat{v}^\dagger(t_0' + \tfrac{\tau'}{2})\, \hat{h}^\dagger(t_0' - \tfrac{\tau'}{2}) + \ell(\tau')\, \hat{v}^\dagger(t_0' + \tfrac{\tau'}{2})\, \hat{v}^\dagger(t_0' - \tfrac{\tau'}{2}) \\ & + \rho(\tau')\, \hat{h}^\dagger(t_0' + \tfrac{\tau'}{2})\, \hat{h}^\dagger(t_0' - \tfrac{\tau'}{2}) \, \Big\} |0\rangle \,, \end{aligned} \tag{6.14}$$

where $\hat{v}^\dagger(t), \hat{v}(t), \hat{h}^\dagger(t)$ and $\hat{h}(t)$ are the creation and annihilation operators for vertically and horizontally polarized photons respectively at time t. One can further express $q(\tau)$ as a mixture of a complex probability amplitude for correlated pairs $\nu(\tau)$ and a background coming from uncorrelated pairs $\chi e^{i\xi}$, where the phase angle ξ is to be averaged over at the end of the calculation. A state is maximally entangled if $\nu(\tau) = \nu(-\tau)$.

Assuming that the backgrounds χ, ℓ and ρ are Poissonian, one can describe them in terms of write $\langle N_w \rangle$ and read $\langle N_r \rangle$ photon rates:

$$\chi \;=\; \sqrt{\langle N_w \rangle \langle N_r \rangle}\,, \tag{6.15a}$$

$$\ell \;=\; \sqrt{\langle N_w \rangle^2}\,, \tag{6.15b}$$

$$\rho \;=\; \sqrt{\langle N_r \rangle^2}\,. \tag{6.15c}$$

$\nu(\tau)$ and $\nu(-\tau)$, on the other hand, are related to Hong-Ou-Mandel interference fringe curves. To back out these two complex probability amplitudes, one can average the two fringe curves from Fig. 6-5, and fit the averaged curve $|\Delta(\tau)|^2$ to

$$|\Delta(\tau)|^2 = A_0 + A_1 \cos 2\phi + A_2 \sin 2\phi + A_3 \cos \phi\,, \tag{6.16}$$

where the fit coefficients A_i are expressions of $\nu(\pm\tau), \chi, \ell$ and ρ.

Equipped with values for almost all the parameters ($Q(t_0)$, being proportional

to the rate of photon pairs, can be left as a variable without affecting the final results), one can calculate the relevant cross correlation $g_{\alpha\beta}$, which in turn gives $E(\alpha, \beta)$ and eventually S. Besides S, another relevant quantity that may be used to quantify entanglement is the entanglement fidelity f_ε, which is the overlap between the maximally entangled state and ψ.

The final results of the calculation are $S = 2.3 \pm 0.2$ and $f_\varepsilon = 0.81 \pm 0.09$. These values show that we should observe a violation of Bell's inequality in a realization of the EPR experiment, i.e. our photons are polarization-time entangled (albeit not maximally entangled).

Chapter 7

Conclusion and Outlook

We have managed to generate pairs of write and read photons, highly correlated in a non-classical manner. The mechanism for generating pairs is well-understood, and we can explain many features of the intensity cross correlations $g_{wr}(\tau)$ and $g_{hom}(\tau)$. We have also subjected these correlated photon pairs to applications like interferometry, which shows promise to perform at a precision beyond the shot noise limit of standard interferometers. We can even entangle the polarizations of photon pairs with modes of time via a different optical pumping scheme.

What next? Quantum cryptography and quantum teleportation are among a whole host of "quantum games" we can now try to play using the new source of entangled photon pairs. However, it is not so refreshing to repeat these protocols that have already been realized with parametric down converters. It is in fact misleading to think of the collectively coupled cesium atoms as another parametric down converter. It is not. The atoms-cavity system has many more capabilities. Most notably, it has quantum memory.

Quantum memory is the reason behind our ability to generate single photons in the first place. This thesis has illustrated the transition from generating one-photon to two-photon Fock states. How about $|n\rangle = |3\rangle, |4\rangle$, and so on? It appears that it is possible to generate these higher-number states using the atoms-cavity system. Akin to holography, one can send in write laser pulses from various directions within the horizontal plane perpendicular to the cavity axis (see Fig. 7-1). These laser pulses

write excitations into the atomic ensemble that are to be "read out" later, either one-by-one by switching on each counter-propagating read laser pulse individually, or altogether to create a n-photon Fock state by turning on all read laser pulses at once.

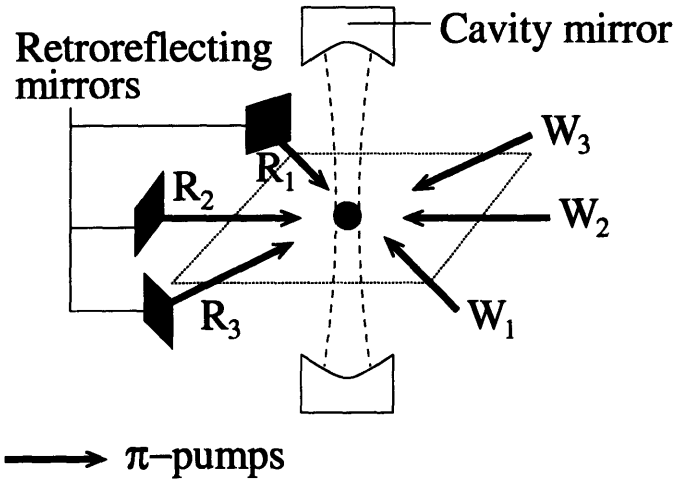

Figure 7-1: Setup for holographic storage of atomic excitations.

Of course, the actual implementation of such a holographic storage device is not as trivial as it sounds. Efficient generation of either n 1-photon Fock states or n-photon Fock states requires fast optical switches, some form of feedback between the detection of a write photon and the switch for read laser pulses, and most importantly, longer coherence times within the atomic ensemble. The coherence time, which governs how long these excitations may be stored, is only $\sim$ 600 ns for the photon-pair setup described in this thesis, although coherence times as long as 3 μs have been reported with an older setup [2]. The 600 ns limit on the coherence time comes from two-photon recoil of atoms that interact with the write pump beam. Presently, work is underway to improve the coherence time by sending in write laser beams at small angles to the cavity axis, which would reduce the amount of two-photon recoil in the atomic cloud.

Appendix A

Quantitative Estimation of Degree of Polarization-Time Entanglement

This section is intended for the more theoretically-inclined readers, who are curious about the nitty-gritty calculations I carried out to predict by how much the polaization-time entangled pairs would violate Bell's inequality.

We start with the most general state of photon pairs after the quarter-waveplate, described in terms of creation and annihilation operators for vertically $(\hat{v}^\dagger, \hat{v})$ and horizontally $(\hat{h}^\dagger, \hat{h})$ polarized photons:

$$\begin{aligned} |\psi\rangle \;=\; & \int dt_0' Q(t_0') \int d\tau' \Big\{ \, q(\tau')\, \hat{v}^\dagger(t_0' + \tfrac{\tau'}{2})\, \hat{h}^\dagger(t_0' - \tfrac{\tau'}{2}) + \ell(\tau')\, \hat{v}^\dagger(t_0' + \tfrac{\tau'}{2})\, \hat{v}^\dagger(t_0' - \tfrac{\tau'}{2}) \\ & + \rho(\tau')\, \hat{h}^\dagger(t_0' + \tfrac{\tau'}{2})\, \hat{h}^\dagger(t_0' - \tfrac{\tau'}{2}) \, \Big\} |0\rangle \; . \end{aligned} \tag{A.1}$$

We remind the reader that $Q(t_0')$ is the probability amplitude for photon pairs to arrive at the polarizing beam splitter at time t_0', and $q(\tau')$ is the probability amplitude that the write and read photons of a given pair are spaced by time τ'. For a maximally entangled state, $q(\tau) = q(-\tau)$ for all τ. By including $\ell(\tau')$ and $\rho(\tau')$ in $|\psi\rangle$, we allow for the possibility that not all photons incident on the polarizing beam splitter come in write-read pairs.

In general, when we detect cross correlations between SPCMs, we are effectively acting on state $|\psi\rangle$ with annihilation operators $\hat{h}$ and $\hat{v}$. Here are some useful algebraic

simplifications that we can employ in later calculations:

$$\begin{aligned} & \hat{v}(t_0+\tfrac{\tau}{2})\,\hat{h}(t_0-\tfrac{\tau}{2})\,\hat{v}^\dagger(t_0'+\tfrac{\tau'}{2})\,\hat{h}^\dagger(t_0'-\tfrac{\tau'}{2})\,|0\rangle \\ = \;& \delta\left(t_0-t_0'+\tfrac{\tau-\tau'}{2}\right)\delta\left(t_0-t_0'-\tfrac{\tau-\tau'}{2}\right)|0\rangle \\ = \;& \delta(t_0-t_0')\,\delta(\tau-\tau')\,|0\rangle\;, \end{aligned} \tag{A.2}$$

which implies

$$\int dt_0' \int d\tau' \ell(\tau')\,\hat{v}_{t_1}\,\hat{v}_{t_2}\,\hat{v}^\dagger_{t_1'}\,\hat{v}^\dagger_{t_2'} = \ell(\tau)+\ell(-\tau)\,, \tag{A.3a}$$

$$\int dt_0' \int d\tau' \rho(\tau')\,\hat{h}_{t_1}\,\hat{h}_{t_2}\,\hat{h}^\dagger_{t_1'}\,\hat{h}^\dagger_{t_2'} = \rho(\tau)+\rho(-\tau)\,, \tag{A.3b}$$

$$\int dt_0' \int d\tau' q(\tau')\,\hat{h}_{t_1}\,\hat{v}_{t_2}\,\hat{v}^\dagger_{t_1'}\,\hat{h}^\dagger_{t_2'} = q(-\tau)\,, \tag{A.3c}$$

$$\int dt_0' \int d\tau' q(\tau')\,\hat{v}_{t_1}\,\hat{h}_{t_2}\,\hat{v}^\dagger_{t_1'}\,\hat{h}^\dagger_{t_2'} = q(\tau)\,. \tag{A.3d}$$

To make the notation less unwieldy, the arguments $(t_0+(\tau/2))$ and $(t_0-(\tau/2))$ have been replaced by their respective subscripts t_1 and t_2 (and similarly for their primed counterparts) in Eq. (A.3).

For convenience, we define the following quantities:

$$\bar{q}(\tau) \equiv \frac{1}{2}(q(\tau)+q(-\tau))\,, \tag{A.4a}$$

$$\tilde{q}(\tau) \equiv \frac{1}{2}(q(\tau)-q(-\tau))\,, \tag{A.4b}$$

$$\bar{\ell}(\tau) \equiv \frac{1}{2}(\ell(\tau)+\ell(-\tau))\,, \tag{A.4c}$$

$$\bar{\rho}(\tau) \equiv \frac{1}{2}(\rho(\tau)+\rho(-\tau))\,. \tag{A.4d}$$

Furthermore, we can break down $\bar{q},\tilde{q}$ into the complex probability amplitudes $\bar{\nu},\tilde{\nu}$ pertaining to the entangled photon pairs, and some τ-independent background of uncorrelated photons $\chi e^{i\xi}$:

$$\bar{q}(\tau) = \bar{\nu}(\tau)+\chi e^{i\xi}\,, \tag{A.5}$$

$$\tilde{q}(\tau) = \tilde{\nu}(\tau)\,, \tag{A.6}$$

where the phase $e^{i\xi}$ will be averaged away at the end of the calculation. Here, we have assumed that both $q(\tau)$ and $q(-\tau)$ have the same background $\chi e^{i\xi}$, hence their antisymmetric combination $\tilde{q}(\tau)$ contains no background term.

We can quantify the degree of entanglement between photons either with the entanglement fidelity f_ε, or with the extent to which Bell's inequality can be violated. The fidelity f_ε is defined to be the overlap between $|\psi\rangle$ and the maximally entangled state $|\varepsilon\rangle$:

$$|\varepsilon\rangle = \int dt_0 Q(t_0) \int d\tau \bar{q}(\tau) \hat{v}^\dagger(t_0 + \tfrac{\tau}{2}) \hat{h}^\dagger(t_0 - \tfrac{\tau}{2}) |0\rangle \,, \tag{A.7}$$

$$\Rightarrow f_\varepsilon = \langle\varepsilon|\psi\rangle = \frac{\int d\tau \{|q(\tau)|^2 + |q(-\tau)|^2 + q^*(\tau)q(-\tau) + q^*(-\tau)q(\tau)\}/4}{\int d\tau |q(\tau)|^2} \tag{A.8}$$

On the other hand, any violation of Bell's inequality can be calculated from the following quantities:

$$S = |E(\alpha,\beta) - E(\alpha',\beta)| + |E(\alpha',\beta') + E(\alpha,\beta')| \; (> 2 \text{ if entangled}) \,, \tag{A.9a}$$

$$\text{where} \quad E(\alpha,\beta) = \frac{g_{\alpha\beta} + g_{\alpha^\perp\beta^\perp} - g_{\alpha^\perp\beta} - g_{\alpha\beta^\perp}}{g_{\alpha\beta} + g_{\alpha^\perp\beta^\perp} + g_{\alpha^\perp\beta} + g_{\alpha\beta^\perp}} \,. \tag{A.9b}$$

$g_{\alpha\beta}(\tau)$ is the intensity cross correlation measured between detectors aligned at angles α and β away from the horizontal axis. Using Eq. (A.1) and the definitions

$$\hat{\alpha} \equiv \hat{h}\cos\alpha + \hat{v}\sin\alpha \,, \tag{A.10a}$$

$$\hat{\beta} \equiv \hat{h}\cos\beta + \hat{v}\sin\beta \,, \tag{A.10b}$$

we can derive $g_{\alpha\beta}(\tau)$ in terms of $q(\tau), q(-\tau), \bar{\rho}(\tau)$ and $\bar{\ell}(\tau)$:

$$\begin{aligned} g_{\alpha\beta}(\tau) &= \left| [\hat{\alpha}_{t_1} \hat{\beta}_{t_2} |\psi\rangle] \right|^2 \\ &= | \, 2\bar{\rho}(\tau)\cos\alpha\cos\beta + 2\bar{\ell}(\tau)\sin\alpha\sin\beta + q(-\tau)\cos\alpha\sin\beta \\ &\quad + q(\tau)\sin\alpha\cos\beta \, |^2 \end{aligned} \tag{A.11}$$

Quantifying the degree of entanglement, be it in terms of the fidelity f_ε or Bell state

parameter S, therefore reduces to a problem of estimating the probability amplitudes $q(\tau), q(-\tau)$ and backgrounds $\ell(\tau), \rho(\tau)$ that parameterize the general state $|\psi\rangle$. These estimates can be backed out from existing data, as we shall show in the next few paragraphs.

Firstly, we assume that the backgrounds comprising uncorrelated write-read, write-write and read-read photon pairs are Poissonian and independent of τ. The backgrounds can then be expressed in terms of the average rates of arrival of write $\langle N_w \rangle$ and read $\langle N_r \rangle$ photons:

$$\chi = \sqrt{\langle N_w \rangle \langle N_r \rangle} \tag{A.12a}$$

$$\ell = \sqrt{\langle N_w \rangle^2} \tag{A.12b}$$

$$\rho = \sqrt{\langle N_r \rangle^2} \tag{A.12c}$$

Next, we relate the probability amplitudes $\bar{\nu}$ and $\tilde{\nu}$ to the Hong-Ou-Mandel interference fringes measured with the variable retarder (see Fig. 5-3). We remind the reader that after the retarder, photons polarized along the two retarder axes get a relative phase shift ϕ, i.e.

$$s \rightarrow s' = se^{i\phi/2} = \frac{v-h}{\sqrt{2}} e^{i\phi/2}, \tag{A.13a}$$

$$f \rightarrow f' = fe^{-i\phi/2} = \frac{v+h}{\sqrt{2}} e^{-i\phi/2}. \tag{A.13b}$$

The polarizing beam splitter after the retarder converts the basis of measurement back to h and v:

$$h' = \frac{f'-s'}{\sqrt{2}} = -iv \sin\frac{\phi}{2} + h\cos\frac{\phi}{2}, \tag{A.14a}$$

$$v' = \frac{f'+s'}{\sqrt{2}} = v\cos\frac{\phi}{2} - ih\sin\frac{\phi}{2}. \tag{A.14b}$$

Hence, after the polarizing beam splitter, the photon pairs are described by the state

$$
\begin{aligned}
|\psi\rangle \rightarrow \int dt_0' \, Q(t_0') \int d\tau' \Big\{ & [\, iq(\tau') \frac{\sin\phi}{2} + \ell \cos^2\frac{\phi}{2} - \rho \sin^2\frac{\phi}{2} \,]\, \hat{v}^\dagger_{t_1'}\, \hat{v}^\dagger_{t_2'} \\
& + [\, iq(\tau') \frac{\sin\phi}{2} - \ell \sin^2\frac{\phi}{2} + \rho \cos^2\frac{\phi}{2} \,]\, \hat{h}^\dagger_{t_1'}\, \hat{h}^\dagger_{t_2'} \\
& + [\, q(\tau') \cos^2\frac{\phi}{2} + i(\rho+\ell) \frac{\sin\phi}{2} \,]\, \hat{v}^\dagger_{t_1'}\, \hat{h}^\dagger_{t_2'} \\
& + [\, -q(\tau') \sin^2\frac{\phi}{2} + i(\rho+\ell) \frac{\sin\phi}{2} \,]\, \hat{h}^\dagger_{t_1'}\, \hat{v}^\dagger_{t_2'} \Big\} |0\rangle \\
= \int dt_0' \, Q(t_0') \int d\tau' & \Big\{ \Upsilon(\tau')\, \hat{v}^\dagger_{t_1'}\, \hat{v}^\dagger_{t_2'} + \Theta(\tau')\, \hat{h}^\dagger_{t_1'}\, \hat{h}^\dagger_{t_2'} + \Delta(\tau')\, \hat{v}^\dagger_{t_1'}\, \hat{h}^\dagger_{t_2'} \Big\} |0\rangle \,, \qquad \text{(A.15)}
\end{aligned}
$$

$$
\text{where} \quad \Delta(\tau') = \bar{q}(\tau') \cos\phi + \tilde{q}(\tau') + i(\bar{\rho} + \bar{\ell}) \sin\phi \,. \qquad \text{(A.16)}
$$

The quantity $|\Delta(\tau)|^2$ describes the Hong-Ou-Mandel interference fringes. Substituting Eqs. (A.4)–(A.6) into Eq. (A.16) and averaging over the phase angle ξ yields

$$
\begin{aligned}
|\Delta(\tau)|^2 &= \frac{1}{2\pi} \int_0^{2\pi} d\xi \left| (\bar{\nu}(\tau) + \chi e^{i\xi}) \cos\phi + \tilde{\nu}(\tau) + i\bar{\mu} \sin\phi \right|^2 \\
&= \frac{1}{2}(|\bar{\nu}(\tau)|^2 + \chi^2 + \bar{\mu}^2 + 2|\tilde{\nu}(\tau)|^2) + \frac{1}{2}(|\bar{\nu}(\tau)|^2 + \chi^2 - \bar{\mu}^2) \cos 2\phi \\
&\quad + \bar{\mu}\, \mathrm{Im}[\bar{\nu}(\tau) + \tilde{\nu}(\tau)] \sin 2\phi + 2\, \mathrm{Re}[\bar{\nu}(\tau)^* \tilde{\nu}(\tau)] \cos\phi \,, \qquad \text{(A.17)}
\end{aligned}
$$

where $\bar{\mu} = \bar{\ell} + \bar{\rho}$. Since we are trying to demonstrate polarization-*time* entanglement, we are interested in the interference fringes obtained from analyzing $g_{wr,\psi}(\tau = \pm\tau_0)$ where $\tau_0 \neq 0$. Hence, one can average the two fringe curves from Fig. 6-5, fit the averaged curve to Eq. (A.17), and solve for the probability amplitudes in terms of the fit coefficients. As a sanity check, we can substitute $q(\tau) = q(-\tau)$ (or equivalently, $\nu(\tau) = \nu(-\tau)$) into Eq. (A.17) to obtain zero for the coefficient of $\cos\phi$, in the case of a maximally entangled state. This means that both Hong-Ou-Mandel fringes will look symmetrical about $\phi \approx 90°$, which is what we expect for perfect entanglement.

Table A.1 gives the fit coefficients A_i of the averaged interference fringe curve, along with the calculated backgrounds and probability amplitudes $\bar{\nu}(\tau)$, $\tilde{\nu}(\tau)$. Two physical solutions, corresponding to two branch cuts, are possible for each probability amplitude. Substituting the values from Table A.1 into Eqs. (A.8), (A.11) and (A.9),

we obtain the final results $f_\varepsilon = 0.81 \pm 0.09$ and $S = 2.3 \pm 0.2$.

Table A.1: Hong-Ou-Mandel interference fringe fit coefficients, estimated probability amplitudes, and estimated backgrounds.

$|\Delta|^2 = A_0 + A_1 \cos 2\phi + A_2 \sin 2\phi + A_3 \cos \phi$

A_0	A_1	A_2	A_3
9.24 ± 0.35	6.90 ± 0.41	1.67 ± 0.50	0.31 ± 0.55

Estimated probability amplitudes $\bar{\nu} = |\bar{\nu}|e^{i\varpi}$, $\tilde{\nu} = |\tilde{\nu}|e^{i\vartheta}$

$\lvert\bar{\nu}\rvert$	ϖ	$\lvert\tilde{\nu}\rvert$	ϑ
$(0.6 \pm 0.3) \times 10^{-3}$	1.19 ± 0.07	$(0.2 \pm 0.1) \times 10^{-3}$	2.7 ± 0.1
$(0.6 \pm 0.3) \times 10^{-3}$	1.95 ± 0.07	$(0.2 \pm 0.1) \times 10^{-3}$	0.4 ± 0.1

Estimated background rates into 20 ns bins

χ	ℓ	ρ
6.42×10^{-5}	7.28×10^{-5}	5.66×10^{-5}

Bibliography

[1] M. J. Holland and K. Burnett. Interferometric detection of optical phase shifts at the Heisenberg limit. *Phys. Rev. Lett.*, 71:1355, 1993.

[2] A. T. Black, J. K. Thompson, and V. Vuletić. On-demand superradiant conversion of atomic spin gratings into single photons with high efficiency. *Phys. Rev. Lett.*, 95:133601, 2005.

[3] T. Kiguchi, A. Uematsu, M. Kitano, and H. Ogura. Grating external cavity diode lasers with broad tunable range and narrow spectral linewidth for high-resolution spectroscopy. *Jpn. J. Appl. Phys*, 35:5890, 1996.

[4] J. K. Thompson, J. Simon, H. Loh, and V. Vuletić. A high-brightness source of narrowband, identical photon pairs for quantum information. *Submitted for publication*, 2006.

[5] P. G. Kwiat, K. Mattle, H. Weinfurter, and A. Zeilinger. New high-intensity source of polarization-entangled photon pairs. *Phys. Rev. Lett.*, 75:4337, 1995.

[6] A. T. Black. *Collective atom-light interactions applied to laser cooling and quantum communications.* PhD thesis, Stanford University, 2005.

[7] A. Kuzmich and L. Mandel. Sub-shot-noise interferometric measurements with two-photon states. *Quantum Semiclass. Optics*, 10:493, 1998.

[8] A. Aspect, P. Grangier, and G. Roger. Experimental realization of Einstein-Podolsky-Rosen-Bohm gedankenexperiment: a new violation of Bell's inequalities. *Phys. Rev. Lett.*, 49:91, 1982.

[9] A. K. Ekert. Quantum cryptography based on Bell's theorem. *Phys. Rev. Lett.*, 67:661, 1991.

[10] D. C. Burnham and D. L. Weinberg. Observation of simultaneity in parametric production of optical photon pairs. *Phys. Rev. Lett.*, 25:84, 1970.

[11] L.-M. Duan, M. D. Lukin, J. I. Cirac, and P. Zoller. Long-distance quantum communication with atomic ensembles and linear optics. *Nature*, 414:413, 2001.

[12] H. Loh, Y.-J. Lin, I. Teper, M. Cetina, J. Simon, J. K. Thompson, and V. Vuletić. Influence of grating parameters on the linewidths of external-cavity diode lasers. *Submitted for publication*, 2006.

[13] C. E. Wieman and L. Hollberg. Using diode lasers for atomic physics. *Rev. Sci. Instrum.*, 62:1, 1991.

[14] L. Ricci, M. Weidemüller, T. Esslinger, A. Hemmerich, C. Zimmermann, V. Vuletić, W. König, and T. W. Hänsch. A compact grating-stabilized diode laser system for atomic physics. *Opt. Commun.*, 117:541, 1995.

[15] H. Patrick and C. E. Wieman. Frequency stabilization of a diode laser using simultaneous optical feedback from a diffraction grating and a narrowband Fabry-Perot cavity. *Rev. Sci. Instrum.*, 62:2593, 1991.

[16] Q. A. Turchette, N. P. Georgiades, C. J. Hood, H. J. Kimble, and A. S. Parkins. Squeezed excitation in cavity QED: experiment and theory. *Phys. Rev. A*, 58:4056, 1998.

[17] D. M. Harber and M. V. Romalis. Measurement of the scalar stark shift of the $6^1S_0 \rightarrow 6^3P_1$ transition in Hg. *Phys. Rev. A*, 63:013402, 2001.

[18] B. Dahmani, L. Hollberg, and R. Drullinger. Frequency stabilization of semiconductor lasers by resonant optical feedback. *Opt. Lett.*, 12:876, 1987.

[19] S. Saito, O. Nilsson, and Y. Yamamoto. Oscillation center frequency tuning, quantum FM noise, and direct frequency modulation characteristics in external grating loaded semiconductor lasers. *IEEE J. Quantum Electron.*, 18:961, 1982.

[20] K. Kikuchi and T. Okoshi. Simple formula giving spectrum-narrowing ratio of semiconductor-laser output obtained by optical feedback. *Electron. Lett.*, 18:10, 1982.

[21] E. Patzak, H. Olesen, A. Sugimura, S. Saito, and T. Mukai. Spectral linewidth reduction in semiconductor lasers by an external cavity with weak optical feedback. *Electron. Lett.*, 19:938, 1983.

[22] E. Patzak, A. Sugimura, S. Saito, T. Mukai, and H. Olesen. Semiconductor laser linewidth in optical feedback configurations. *Electron. Lett.*, 19:1026, 1983.

[23] G. Agrawal. Line narrowing in a single-mode injection laser due to external optical feedback. *IEEE J. Quantum Electron.*, 20:468, 1984.

[24] H. Sato and J. Ohya. Theory of spectral linewidth of external cavity semiconductor lasers. *IEEE J. Quantum Electron.*, 22:1060, 1986.

[25] B. Tromborg, H. Olesen, X. Pan, and S. Saito. Transmission line description of optical feedback and injection locking for Fabry-Perot and DFB lasers. *IEEE J. Quantum Electron.*, 23:1875, 1987.

[26] M. W. Fleming and A. Mooradian. Spectral characteristics of external-cavity controlled semiconductor lasers. *IEEE J. Quantum Electron.*, 17:44, 1981.

[27] R. Wyatt and W. J. Devlin. 10 khz linewidth 1.5 μm InGaAsP external cavity laser with 55 nm tuning range. *Electron. Lett.*, 19:110, 1983.

[28] R. Wyatt. Spectral linewidth of external cavity semiconductor lasers with strong, frequency-selective feedback. *Electron. Lett.*, 21:658, 1985.

[29] J. O. Binder, G. D. Cormack, and A. Somani. Intermodal tuning characteristics of an InGaAsP laser with optical feedback from an external-grating reflector. *IEEE J. Quantum Electron.*, 26:1191, 1990.

[30] G. Genty, A. Gröhn, H. Talvitie, M. Kaivola, and H. Ludvigsen. Analysis of the linewidth of a grating-feedback GaAlAs laser. *IEEE J. Quantum Electron.*, 36:1193, 2000.

[31] G. Genty, M. Kaivola, and H. Ludvigsen. Measurements of linewidth variations within external-cavity modes of a grating-cavity laser. *Opt. Commun.*, 203:295, 2002.

[32] R. Lang and K. Kobayashi. External optical feedback effects on semiconductor injection laser properties. *IEEE J. Quantum Electron.*, 16:347, 1980.

[33] I. D. Henning. Linewidth broadening in semiconductor lasers due to mode competition noise. *Electron. Lett.*, 19:935, 1983.

[34] H. Talvitie, A. Pietiläinen, H. Ludvigsen, and E. Ikonen. Passive frequency and intensity stabilization of extended-cavity diode lasers. *Rev. Sci. Instrum.*, 68:1, 1997.

[35] C. Audoin. Frequency metrology. In A. F. Milone, P. Giacomo, and F. Leschiutta, editors, *Int'l School of Physics E. Fermi*, pages 169–219. North-Holland, Amsterdam, 1980.

[36] H. Li and H. R. Telle. Efficient frequency noise reduction of GaAlAs semiconductor lasers by optical feedback from an external high-finesse resonator. *IEEE J. Quantum Electron.*, 25:257, 1989.

[37] T. Laurila, T. Joutsenoja, R. Hernberg, and M. Kuittinen. Tunable external-cavity diode laser at 650 nm based on a transmission diffraction grating. *Appl. Opt.*, 41:5632, 2002.

[38] K. L. Corwin, Z.-T. Lu, C. F. Hand amd R. J. Epstein, and C. E. Wieman. Frequency-stabilized diode laser with the Zeeman shift in an atomic vapor. *Appl. Opt.*, 37:3295, 1998.

[39] C. J. Hawthorn, K. P. Weber, and R. E. Scholten. Littrow configuration tunable external cavity diode laser with fixed direction output beam. *Rev. Sci. Instrum.*, 72:4477, 2001.

[40] R. Loudon. *The quantum theory of light.* Oxford University Press, 2000.

[41] E. M. Purcell. Spontaneous emission probabilities at radio frequencies. *Phys. Rev.*, 69:681, 1946.

[42] A. E. Siegman. *Lasers.* University Science Books, 1986.

[43] M. O. Scully and M. S. Zubairy. *Quantum optics.* Cambridge University Press, 2002.

[44] R. H. Dicke. Coherence in spontaneous radiation processes. *Phys. Rev.*, 93:99, 1954.

[45] Y. Yamamoto and A. Imamamoglu. *Mesoscopic quantum optics.* John Wiley & Sons, Inc., 1999.

[46] C. Cohen-Tannoudji, J. Dupont-Roc, and G. Grynberg. *Atom-photon interactions: basic processes and applications.* John Wiley & Sons, Inc., 1992.

[47] M. O. Scully. Resolving conundrums in lasing without inversion via exact solutions to simple models. *Quantum Opt.*, 6:203, 1994.

[48] R. P. Feynman and A. R. Hibbs. *Quantum mechanics and path integrals.* McGraw-Hill, 1964.

[49] M. J. Childress. Narrow frequency-band laser with optical feedback. Bachelor's thesis, Massachusetts Institute of Technology, 2005.

[50] J. F. Clauser. Experimental distinction between the quantum and classical field-theoretic predictions for the photoelectric effect. *Phys. Rev. D*, 9:853, 1974.

[51] C. K. Hong, Z. Y. Ou, and L. Mandel. Measurement of subpicosecond time intervals between two photons by interference. *Phys. Rev. Lett.*, 59:2044, 1987.

[52] M. V. Berry. Quantal phase factors accompanying adiabatic changes. *Proc. R. Soc. Lond. A*, 392:45, 1984.

[53] C. A. Sackett, D. Kielpinski, B. E. King, C. Langer, V. Meyer, C. J. Myatt, M. Rowe, Q. A. Turchette, W. M. Itano, D. J. Wineland, and C. Monroe. Experimental entanglement of four particles. *Nature*, 404:256, 2000.

[54] M. D'Angelo, M. V. Chekhova, and Y. Shih. Two-photon diffraction and quantum lithography. *Phys. Rev. Lett.*, 87:013602, 2001.

[55] K. S. Thorne. Gravitational-wave research: current status and future prospects. *Rev. Mod. Phys.*, 52:285, 1980.

[56] D. T. Pegg and S. M. Barnett. Tutorial review: quantum optical phase. *J. Mod. Optics*, 44:225, 1997.

[57] C. M. Caves. Quantum-mechanical radiation-pressure fluctuations in an interferometer. *Phys. Rev. Lett.*, 45:75, 1980.

[58] C. M. Caves. Quantum-mechanical noise in an interferometer. *Phys. Rev. D*, 23:1693, 1981.

[59] L.-A. Wu, H. J. Kimble, J. L. Hall, and H. Wu. Generation of squeezed states by parametric down conversion. *Phys. Rev. Lett.*, 57:2520, 1986.

[60] M. Xiao, L.-A. Wu, and H. J. Kimble. Precision measurement beyond the shot-noise limit. *Phys. Rev. Lett.*, 59:278, 1987.

[61] B. Yurke, S. L. McCall, and J. R. Klauder. SU(2) and SU(1,1) interferometers. *Phys. Rev. A*, 33:4033, 1986.

[62] C. H. Bennett, G. Brassard, C. Crépeau, R. Josza, A. Peres, and W. K. Wootters. Teleporting an unknown quantum state via dual classical and Einstein-Podolsky-Rosen channels. *Phys. Rev. Lett.*, 70:1895, 1993.

[63] J. I. Cirac and P. Zoller. Quantum computations with cold trapped ions. *Phys. Rev. Lett.*, 74:4091, 1995.

[64] M. A. Nielsen and I. L. Chuang. *Quantum computation and quantum information.* Cambridge University Press, 2000.

[65] Z. Y. Ou and L. Mandel. Violation of Bell's inequality and classical probability in a two-photon correlation experiment. *Phys. Rev. Lett.*, 61:50, 1988.

[66] D. J. Griffiths. *Introduction to quantum mechanics.* Prentice-Hall, Inc., 1994.

[67] A. Einstein, B. Podolsky, and N. Rosen. Can quantum-mechanical description of physical reality be considered complete? *Phys. Rev.*, 47:777, 1935.

[68] J. F. Clauser, M. A. Horne, A. Shimony, and R. A. Holt. Proposed experiment to test local hidden-variable theories. *Phys. Rev. Lett.*, 23:880, 1969.

[69] A. Aspect, P. Grangier, and G. Roger. Experimental tests of realistic local theories via Bell's theorem. *Phys. Rev. Lett.*, 47:460, 1981.

[70] W. J. Munro, K. Nemoto, and A. G. White. The Bell inequality: a measure of entanglement? *J. Mod. Optics*, 48:1239, 2001.